Die approbierte Originalversion dieser Diplom-/Masterarbeit ist in der Hauptbibliothek der Technischen Universität Wien aufgestellt und zugänglich.
http://www.ub.tuwien.ac.at

The approved original version of this diploma or master thesis is available at the main library of the Vienna University of Technology.
http://www.ub.tuwien.ac.at/eng

TECHNISCHE UNIVERSITÄT WIEN
Vienna | Austria

Monitoring of Heart- and Respiration Rate by MEMS with Organic Optoelectronic Readout

DIPLOMA THESIS

submitted to

Institute of Sensor and Actuator Systems

TU Wien

under the supervision of

Ao.Univ.Prof. Dipl.-Ing. Dr.techn. Franz Keplinger

and

Dipl.-Ing. Dr.techn. Andreas Kainz

by

Günter Hammer, BSc

Matr. No.: 01030272

to achieve the university degree of

Diplom-Ingenieur

Master's degree programme: Biomedical Engineering

Wien, April 2018

Contents

Abstract **v**

Kurzfassung **vi**

Danksagung **vii**

1. Introduction **1**

2. Theory **3**
2.1. Pulse measurement 3
2.2. Respiration rate measurement 4
2.3. Organic Optoelectronics 6
2.4. Noise basics 9
2.4.1. Overview 10
2.4.2. Comparing Intrinsic and Extrinsic noise sources 11
2.4.3. Shot noise 12
2.4.4. Thermal noise 13
2.4.5. Diffusion noise 15
2.4.6. 1/f Noise (Flicker noise or Excess Noise) 16
2.4.7. Quantum noise 17
2.4.8. Generation-Recombination Noise (G-R Noise) 18
2.4.9. Popcorn (Burst) noise 19
2.4.10. Avalanche noise 19
2.4.11. Noise in different components 20

3. Methods **21**
3.1. Photodetection readout circuit 21
3.1.1. Basic functionality 21
3.1.2. Improving the SNR 23
3.1.3. Offset compensation (Simulation in QUCS) 24
3.1.4. TIA bandwidth 26
3.1.5. TIA stabilisation 27
3.2. The MEMS Sensor 30
3.2.1. MEMS Sensor principle 30
3.2.2. Mathematical model of the mechanical response 31
3.2.3. Sensitivity 34

3.3. Measurement setup 37
3.3.1. MEMS characteristic 37
3.3.2. Analysis of readout circuit noise 40
3.3.3. Heart- and respiration rate 41

4. Results **43**
4.1. Performance of the readout electronics 43
4.2. Results of noise measurements 45
4.3. Comparing inorganic to organic sensor setup 48
4.4. OLED performance 53
4.5. Performance of OPDs with chromium grating 53
4.6. Heart- and respiration rate measurement 56

5. Discussion and outlook **61**

A. MEMS chip sensitivity data **65**

Bibliography **69**

Abstract

In this diploma thesis a displacement-sensitive sensor comprising a micro-electro-mechanical-system (MEMS) chip with organic optoelectronic components is utilised to measure the pulse and respiration rate on humans. The MEMS sensor relies on the deflection of a small silicon oscillator, which is induced by an external mechanical actuation. The readout of the deflection is optical and works via modulation of the light flux passing through the MEMS by the oscillator.
Within the scope of this work, the hitherto used inorganic semiconductors (LED and PD) were replaced with organic ones (OLED and OPD). This should increase the compactness of the sensor and lead to a more homogeneous light distribution. Another task was to improve the signal-to-noise ratio of the readout electronics. An increase of 20 dB could be achieved by adapting electronic components to the low currents produced by photodiodes.
Several MEMS chips were characterised regarding their sensitivity and resonance frequency in order to compare the inorganic to the organic configuration. The organic setup showed a lower sensitivity for all measurements. Amongst other reasons, this can be explained by spatial misalignment between the MEMS chip and the organic semiconductors. In addition, a slow decay of the OLED material was noticed, leading to a steadily degrading sensitivity.
Finally, heart- and respiration rate measurements were conducted with the inorganic and the organic setup. By measurements on the neck, pulse and respiration rate could be determined. Two types of MEMS chips differing in their resonance frequency were investigated for their detection capability. The MEMS chips with lower resonance frequency ($f_\mathrm{r} \sim 250$ Hz) showed good results, whereas the MEMS with higher resonance frequency ($f_\mathrm{r} \sim 620$ Hz) did not. The sensitivity in the respective region of pulse and respiration ($f \lesssim 3$ Hz) was too low for these structures. Analogously to the characterisation of the chips, the organic setup showed a lower sensitivity, and therefore, the signal quality was worse compared to the inorganic case. Nevertheless, the results show that it is possible to monitor pulse and respiration rate with such a sensor, which is promising for further developments.

Kurzfassung

In dieser Diplomarbeit wird ein positionsempfindlicher Sensor, bestehend aus einem MEMS Chip (micro-electro-mechanical-system) mit organischen optoelektronischen Komponenten dazu verwendet, um Puls und Atmungsfrequenz am Menschen zu messen. Der MEMS-Sensor beruht auf der Auslenkung eines kleinen Silizium-Oszillators, hervorgerufen durch eine externe mechanische Anregung. Die Auslenkung wird optisch ausgelesen, indem der Oszillator den Lichtstrom durch den Sensor moduliert und das so entstandene Signal mittels einer Photodiode detektiert wird.
Im Rahmen dieser Arbeit wurden die bisher benutzten anorganischen Halbleiter (LED und PD) durch organische (OLED und OPD) ersetzt. Dadurch sollte der Sensor kompakter und die Lichtverteilung homogener werden. Eine weitere Aufgabe war die Erhöhung des Signal-Rausch-Verhältnisses (SNR) der Detektorschaltung. Durch die Anpassung elektronischer Komponenten an die niedrigen Ströme von Photodioden konnte eine Verbesserung um 20 dB erreicht werden.
Mehrere MEMS Chips wurden bezüglich ihrer Sensitivität und Resonanzfrequenz charakterisiert um die anorganische Konfiguration des Sensors mit der organischen zu vergleichen. Der organische Aufbau zeigte für alle Messungen eine niedrigere Sensitivität. Diese kann unter anderem durch schlechte räumliche Ausrichtung zwischen MEMS Chip und den organischen Halbleitern erklärt werden. Zusätzlich wurde ein langsamer Abbau des OLED Materials beobachtet, was zu einer stetig abnehmenden Sensitivität führte.
Schließlich wurden Puls- und Atemfrequenz-Messungen mit dem anorganischen und organischen Aufbau durchgeführt. Durch Messungen am Hals konnten Herz- und Atemrate bestimmt werden. Zwei Typen von MEMS Chips, die sich in ihrer Resonanzfrequenz unterscheiden, wurden auf ihre Erfassungsfähigkeit untersucht. MEMS Chips mit niedriger Resonanzfrequenz ($f_\mathrm{r} \sim 250$ Hz) lieferten gute Ergebnisse, während MEMS mit hoher Resonanzfrequenz ($f_\mathrm{r} \sim 620$ Hz) schlecht abschnitten. Für diese Strukturen lag die Sensitivität im Bereich von Puls und Atmung ($f \lesssim 2$ Hz) zu niedrig. Analog zu den Charakterisierungen der Chips zeigte der organische Aufbau eine niedrigere Sensitivität, was zu einer schlechteren Signalqualität im Vergleich zum anorganischen Fall führte. Die Ergebnisse zeigten dennoch, dass die Messung von Puls und Atemfrequenz mit solchen Sensoren möglich und vielversprechend für weitere Entwicklungen ist.

Danksagung

An dieser Stelle möchte ich mich bei allen Personen bedanken, die zum Gelingen dieser Diplomarbeit beigetragen haben. Ein großer Dank geht an Prof. Franz Keplinger, der mir die Möglichkeit gab diese Diplomarbeit zu schreiben, zu jeder Zeit ein offenes Ohr hatte und mir mit Rat und Tat zur Seite stand. Weiters möchte ich mich recht herzlich bei Dr. Andreas Kainz bedanken, der während meiner Arbeit im Labor, aber auch während des Verfassens der schriftlichen Dokumentation auf alle meine Fragen eine gute Antwort wusste. Ohne seine Expertise und das sorgfältige Korrekturlesen wäre ein erfolgreicher Abschluss dieser Arbeit wahrscheinlich nicht möglich gewesen. Bedanken möchte ich mich auch beim Team des ISAS, insbesondere bei Dr. Artur Jachimowicz, Dr. Johannes Schalko und Dr. Franz Kohl für ihren Input zur Arbeit und den unzähligen interessanten Diskussionen während der Mittagspausen. Am Institut herrschte immer ein sehr entspanntes und freundschaftliches Arbeitsklima, in dem ich mich sehr wohl fühlte. Dazu beigetragen haben auch die beiden Diplomanden Matthias Kahr und Martin Windisch, bei denen ich mich dafür bedanken möchte.
Mein Studium wäre ohne die Unterstützung und den Rückhalt durch meine Familie nicht möglich gewesen. Danke für das Vertrauen in mich und das ihr mich auf meinem Weg immer begleitet habt und immer da gewesen seid, wenn ich euch brauchte. Ganz besonders bedanken möchte ich mich bei meiner Freundin Katharina, für ihr großes Verständnis für mich und den Mut und die Motivation, die sie mir immer wieder gegeben hat.

1. Introduction

Since their introduction into mass production in the early 1980s, the range of microelectromechanical systems (MEMS) has expanded exponentially and thus, also their field of applications. The micromachined automotive MAP (Manifold Absolute Pressure) sensor used in engine control and the micromachined disposable medical blood pressure sensor were the first mass-produced MEMS products brought on the market [1, 2]. The technological advances in the integrated circuit industry (microlithography, etching, thin film technologies, etc.) accelerated the development of novel sensor concepts, which were also suitable for the often harsh environments in industry and daily life. Examples for the broad field of applications are the airbag-deployment accelerometer, which started high volume production in the 1990s [3], or gyroscopes which are miniature parts of every-day life and are used for orientation and movement control in tablets, smart phones and many other devices. Nowadays, medicine and biology are among the most promising and challenging fields of application for MEMS. Medical devices based on this technology (bioMEMS) are currently being investigated for a broad variety of in vivo and point-of-care implementations. Herein new challenges have to be overcome, such as biocompatibility and minimal tissue response. These were not important in the applications up to now [4].
Their small size, high level of integration and the ability for mass production are some key properties of MEMS sensors, to name only a few advantages. Therefore, they can be manufactured in a very cost-efficient way which also lead to applications in many different areas. An important field of application of MEMS sensors is displacement and acceleration measurement. Various principles to transduce the deflections of such a sensor into an electronic signal exist, e.g. piezoresistive or -electric, capacitive and optical readout methods. In order to receive the best sensor performance, usually the capacitive readout is the method of choice. There, a set of fixed and moveable electrodes form a capacitor which changes its capacity with respect to the external actuation [5, 6]. Nonetheless, this method has drawbacks in practical use, like a small

measurement range at high sensitivities and relatively high mechanical resonance frequencies, which limit the field of applications.
A promising alternative is the optical readout [7, 8, 9]. MEMS sensors of this type are sometimes called MOEMS (micro-opto-electro-mechanical systems) in the literature. The optical readout is contactless, requires no electrical leads on moveable parts of the sensor and enables a galvanic insulation between the transducer and the readout electronics. A major drawback of this detection principle is the problem of integrating the relatively bulky inorganic optoelectronics with the MEMS sensor, because of different semiconductor materials involved [10]. The idea is now to use organic optoelectronics which can be manufactured on much smaller scales and therefore can be integrated with the MEMS chip more tightly.
In this thesis such a MEMS vibration sensor with organic optoelectronic readout is utilised to measure heart- and respiration rate on humans, which is very challenging for inertial sensors. Advantages of this method would be the relatively simple measurement principle and the small size of the sensor. But still a lot of work has to be invested to make this kind of sensors ready for the commercial use and a lot of drawbacks (e.g. sensitivity to vibrations from gait, movement and external shocks) have to be overcome.
The thesis is structured as follows. Chapter 2 gives a general overview of theoretical background relevant for this work. The state-of-the-art of pulse- and respiration measurement as well as basics of inorganic and organic LEDs and photodetectors are summarised. Also different origins of electronic noise are outlined. In Chapter 3, the focus lies on the readout electronics used to detect the sensor signal, the MEMS sensor principle and the various measurement setups necessary to perform the measurements. The results are presented in Chapter 4 and a short discussion and outlook is given in Chapter 5.

2. Theory

2.1. Pulse measurement

The basic function of our heart is to pump blood through our body, achieved by rhythmic contractions of the heart muscle. That is important, because the blood supplies the cells of our body with oxygen and nutrients and is as well responsible for the removal of carbon dioxide and waste products from the cells. The activity of our heart is measured in beats per minute (1/min) or beats per second (Hz) and is called heart rate, pulse or cardiac activity. It is an important vital parameter of our body and can give basic information about the state of health of a person. Thus, physicians have been interested in the heart rate and other biosignals for many centuries and various strategies and devices have developed to measure them. Dr. Robert Ellis Dudgeon (1820 - 1904) invented the first compact portable device for a graphical recording of the radial pressure pulse. The sphygmograph (greek *sphygmos* pulse, *graph* write) was used in medical practice around the world. It consists of a lever with an elastic spring placed on the radial artery. On the other end of the lever a pen records the pulse signal on a moving blackened paper [11].
Since then, many methods to detect the pulse signal have emerged due to the immense technological and medical progress. One of the widest spread methods is the electrocardiogram, which is an electric biosignal. The contraction of the heart muscle is induced by an electric activation started in the sinoatrial node. By applying electrodes on the skin the change in the electric activation can be measured as a voltage change, which shows a repeating pattern related to the rhythmic contraction of the heart. The heart rate as well as distortions in the cardiac activity (cardiac arrhythmia) and other parameters of the heart can be detected by this method. It is used in advanced medical devices for patients surveillance, as well as in simple fitness tracking devices like pulse chest belts.
Another method to detect the heart rate is the optoplethysmogram, an optic biosignal.

Therein, a light source (e.g. an LED) is used to couple light into the body tissue, for example on a finger. On the opposite side of the finger a light detector (e.g. a photodiode) is placed, which registers the light travelled through. The light is modulated while propagating through the different kinds of tissues. The absorption of light depends on the blood volume in an artery and also on the level of blood oxygenation. When the light passes through a pulsatile wave of blood (the radius of the artery is increased), it is absorbed to a higher extent, and the amount of light on the sensor is reduced. On the other hand, the absorption coefficient of deoxygenated blood is higher than the one of oxygenated blood for red light at about 660 nm. Thus, the light signal detected at the photodiode yields information about pulse, blood oxygenation state and also other vital parameters.
A third method is the phonocardiogram, which is an acoustic biosignal and relies on the detection of body sounds. The first and the second heart sound, which are generated by consecutive closures of the heart valves, and sounds which are produced during breathing or snoring are recorded by a chestpiece (used e.g. in a stethoscope), placed on the skin of the thorax. The vibrations of the skin are induced by the body sounds and are converted by a thin diaphragm into sound propagating in the chestpiece. At the other end of the chestpiece a microphone converts the sound waves into an electric signal (condenser microphone). Through this voltage signal the cardiac activity and information about the respiratory cycle can be gained.
These methods are by far not all which are available to detect the cardiac activity. Others are for example the electroplethysmogram (an electric biosignal, based on the detection of pulsatile changes of the electric tissue impedance), magnetocardiogram (a magnetic biosignal, based on the measurement of magnetic field changes due to the electric excitation of the heart) and the mechanocardiogram (a mechanic biosignal, relying on vibrations and skin deformations evoked by pulsating blood vessels). The detailed explanation of all these methods would go beyond the scope of this thesis and, thus, it is referred to the corresponding literature [11, 12].

2.2. Respiration rate measurement

Our lung takes care of the exchange of oxygen (O_2) and carbon dioxide (CO_2) between the blood and the air. CO_2 is released at the alveoli of the lung through its passive diffusion gradient from the blood into the air and O_2 is diffusing passively from the

air into the pulmonary capillaries (because the O_2 concentration of the alveolar air is higher than that of the blood). The oxygen enriched blood flows from the lung into the left atrium of the heart and is pumped via the left ventricle into all parts of the body, where the oxygen is released into the tissue. Air intake is achieved by contraction of the respiratory muscles, which leads to an expansion of the thorax and the lung inside. This way, the air pressure within the lung is decreased which causes air to be sucked in (inspiration). On the other hand, expiration is a passive process, stemming from the relaxation of the respiratory muscles.

The detection of respiratory parameters (e.g. the respiration rate, tidal volume) is important to assess the health status of a person and, therefore, many methods exist to measure them. Only a few methods are briefly introduced here and the interested reader is referred to the literature for more information [11, 12].

Circumference changes of the chest (and also the abdomen) during breathing are registered in the mechanorespirogram (a mechanic biosignal). The signal is recorded via a respiratory belt attached to the skin. The belt comprises a piezoelectric transducer which converts the mechanical tensions and relaxations during inspiration and expiration into a voltage signal respectively. Another mechanical biosignal is used in the spirometry, a method which is quite common in clinical practice to measure basic lung parameters. A mouthpiece is connected to an airflow transducer which records the air flow through the mouth, while nasal airflow is stopped by a clip. Inside the transducer, a tube with a woven screen acts as flow resistance. During inspiration (positive airflow) and expiration (negative airflow) pressure differences occur across the flow resistance, which are proportional to the air flow and are converted into a voltage signal by a pressure sensor. Recording of this signal leads to a periodic waveform from which the respiration rate can be calculated. By integration of the flow signal inspiration and expiration volumes can be gained.

The phonocardiogram (already explained in Sec. 2.1) shows mainly heart sounds from the closure of the heart valves. But also lung sounds are present from normal breathing, which are originating from turbulences in the branching airways of the lung. They have a much lower amplitude than the heart sounds and are therefore more difficult to detect.

Another method to detect respiratory activity is the thermorespirogram, a thermal biosignal. Airflow temperature variations are detected by a thermistor placed in front of the nostrils. During expiration the temperature is normally higher as during inspira-

tion, because of warming up towards the body core temperature (∼37 °C) in the body. These periodic variations of the temperature are translated into voltage changes by the thermistor and enable the detection of the respiration rate.

2.3. Organic Optoelectronics

One can hardly imagine a life without organic optoelectronics today. On the one hand, OLEDs are part of every day devices, such as displays of smart phones, tablets and TVs. On the other hand, organic photodetectors slowly find their way into imaging sensors used in cameras as standalone devices or integrated in smart phones, cars or even optical devices for surgery in medicine [13, 14]. The reasons for their success are the inherent advantages of organic devices compared to inorganic optoelectronics: They are lightweight, semi-transparent, wearable and can be manufactured as thin and flexible structures on large areas. Due to the tremendous progress in printed electronic techniques like spray-coating, stamping and inkjet-printing over the last decades it poses no difficulty to produce large-area devices at very low costs [15]. However, every new technology has to overcome drawbacks too. In the case of organic devices the most prominent ones are limited lifetime and robustness, since the materials are sensitive to oxidation, humidity and high temperatures. Thus, a lot of money has been invested in their research and development to improve the duration and passivation performances [10].

Inorganic and organic optoelectronics rely more or less on the same principle. For emission or absorption of light, an energy gap in the band structure of solid state devices is necessary, whereas in organic devices orbitals take the role of the bands. In inorganic semiconductors the conduction band, where electrons can move freely, lies on a higher energy level as the valence band, where electrons are bound to atoms, but holes can move freely. A pn junction is formed between two oppositely doped semiconductors, with different energy levels of conduction- and valence band. This junction is characterised by a depletion zone (region without free charge carriers) between the n- and p-doped area, which connects the energy levels forming a slope from the p-region down to the n-region energy level (see Figures 2.1a and 2.2a). If a forward voltage is applied on an LED, then this band slope is reduced and a current I_{LED} is flowing. Thus, electrons are injected into the p-region and holes into the n-region, and most of the charge carriers recombine in the depletion zone. By one

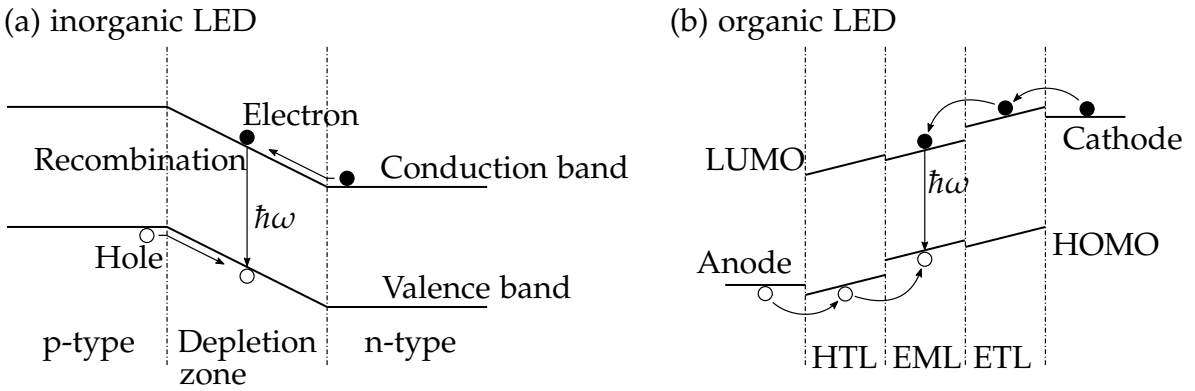

Figure 2.1.: Energy level diagrams of an inorganic LED (a) and an OLED (b). Recombination takes place in the depletion zone in the LED, whereas in the OLED the emissive layer (EML) is the origin of light generation [16].

recombination process one photon (in the optimum case) with the energy $E_{\text{ph}} = \hbar\omega$ is released. The energy (colour) of this light emission depends on the band gap between conduction- and valence band and can therefore be designed by the choice of the semiconductor materials [17].

The function of the valence- and the conduction band are taken over by the HOMO (highest occupied molecular orbital) and LUMO (lowest unoccupied molecular orbital) in the case of organic LEDs, respectively (see Fig. 2.1b). The cathode (Al electrode in this work) releases an electron which is carried by the electron transport layer (ETL) into the emissive layer (EML). There, it forms an exciton (neutral bound electron-hole pair) with a hole and a photon is released by this process. TPBi is used as ETL and the EML, where light generation happens, consists of a CBP polymer with embedded $Ir(mppy)_3$ (responsible for the emission of green light)[10]. Holes are injected at the anode which consists of transparent indium tin oxide (ITO) in this work. They are carried by the hole transport layer (HTL, made of TCTA in this work) into the EML, where they interact with the electrons. An additional layer (consisting of PEDOT:PSS in this work) is needed to interconnect the ITO electrode with the HTL. A glass substrate (transparent for the released light) on which the ITO electrode is structured, finalizes the four layer setup of the OLEDs which are used in this work. As suggested above, the colour of the emission light is determined by the organic material in the EML. It depends on the energy gap between HOMO and LUMO, similar to inorganic semiconductors.

In an inorganic photodiode (PD), a current I_{ph} is generated in the depletion zone by incident photons. The energy of the incoming light needs to be at least equal to the

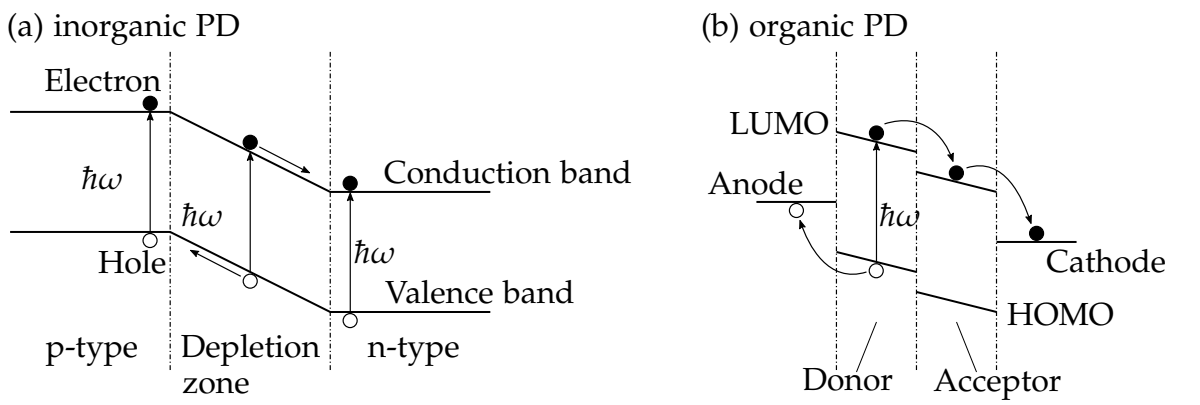

Figure 2.2.: Energy level diagrams of an inorganic PD and the organic counterpart (OPD). Incident light at the depletion zone generates free charge carriers and leads to a photocurrent, proportional to the light power. The same happens in the organic case in principle, where light produces an exciton in the active organic area, which is separated due to the different energy levels of LUMO and HOMO [16].

band gap between conduction and valence band. The absorbed photon generates a pair of charge carriers, which is separated by the electric field in the depletion zone. Thus, the electron moves in the direction of the n-doped zone and the hole in the opposite direction into the p-doped zone, which leads to a current proportional to the incoming light power. High quantum yields for the conversion of photons to free carriers can be reached with inorganic semiconductor materials such as GaAs or InP. A reverse bias applied to the photodiode enlarges the depletion zone and leads to a decrease of the pn junction's capacitance which improves the time response of the diode. Additionally, the region in which generated charge carriers contribute to the photo current is increased. A drawback of this improved time response and the enhanced sensitivity is an increased dark current of the photodiode, which leads to a higher detector noise [18].

The first OPD, which is the organic counterpart, was demonstrated by Kudo and Moriizumi [19] in 1981. A photon is absorbed in the organic semiconductor layer, if it is of equal or greater energy than the energy gap between the orbitals (similar as in inorganic photodiodes). This induces the formation of an exciton as pointed out in Fig. 2.2b. The quantum yield in a homojunction (an active layer consisting of a single material) is low. Therefore, this results in a maximum external quantum efficiency (EQE) of usually around 1%, which is poor[20]. An approach to solve this restriction is to overcome the exciton binding energy by combining an electron donor (D) with an electron acceptor (A) material. The D-A energy offset has to be higher than the exciton

binding energy, in order to enable electron or hole transfer. Two ways exist to realize that requirement: by forming a D-A planar heterojunction (so called bilayer), or by mixing the donor and acceptor materials in a blend to form a distributed heterojunction across the bulk of the thin solid film (bulk heterojunction BHJ)[21, 22].
The OPDs used in this work comprise an active layer composed of a D-A blended system. PCBM is the donor material and corresponds to the n-doped semiconductor in the inorganic PD and P3HT is the acceptor material and takes the role of the p-doped semiconductor. A PEDOT:PSS polymer is used to interconnect the active layer with the transparent ITO electrode, which is patterned on a glass substrate. The incident light on this side of the OPD leads to a photocurrent generated in the active organic layer, whereas on the other side of the active material an aluminium electrode is evaporated [10]. The size of the photosensitive area of the OPD (and of the emitting area of the OLED) is defined by the overlap of the ITO and Al electrodes.

2.4. Noise basics

One aim of this work was to improve the performance of the readout circuit in order to achieve a better SNR. The amplitude of the photocurrent, which is delivered by the PD, is in the pA to nA range. Therefore, high amplification of the photocurrent is necessary to get a reliable signal which can be measured and analysed by subsequent instruments (e.g. oscilloscope, lock-in amplifier). Due to this very low current levels, internal disturbances (e.g. thermal noise from resistors, shot noise from semiconductors) or external disturbances (e.g. interference from electric power lines and electric motors) can easily make the signal unusable. In the worst case, the signal is completely buried in noise and no information can be retrieved from it. From that point of view, it is mandatory to construct an electronic readout circuit which produces the lowest possible noise, with the highest possible amplification of the signal. Following that idea, the SNR will be improved.
In this section, the general basics of noise in electrical circuits are explained and the different fundamental sources of noise are introduced, based on the detailed reference [23].

2.4.1. Overview

Principally, it can be distinguished between two main types of noise, namely intrinsic and extrinsic noise. As the name already indicates, intrinsic noise is generated inside the investigated device. The source of intrinsic noise lies in the discrete nature of charge carriers. A typical example is thermal noise, originating from random motion of electrons inside a conductive material. This motion leads to a temporal agglomeration of electrons at one or the other side of the conductor, which produces a fluctuating voltage which can be measured. The mean value of the fluctuation must be zero, because the motion of the electrons has random nature. Calculating its root mean square leads to the thermal noise voltage

$$v_{\mathrm{tn}} = \sqrt{4k_{\mathrm{B}}T\Delta f R}, \tag{2.1}$$

where $k_{\mathrm{B}} = 1.38 \cdot 10^{-23}$ J/K is the Boltzmann constant, T is the absolute temperature in K, Δf is the bandwidth and R is the resistance.
Other types of intrinsic noise are for example:

- Shot noise: Due to random passage of charge carriers across a barrier of potential
- Flicker or $1/f$ noise: The origin is not understood completely yet, but apparently depends on lattice defects
- Diffusion noise: Results from carrier velocity fluctuations induced by collisions

The most important feature of all types of intrinsic noise is their randomness. In the frequency spectrum, their mechanisms typically yield white noise, which means that the noise power is equally distributed over the whole frequency spectrum. An exception of this property is flicker noise, which has a $1/f$ noise spectrum. Consequently, the noise spectrum increases with decreasing frequency. Noise of such kind is also called pink noise.
Extrinsic noise sources are located outside the investigated device. Therefore, this sources are also called extraneous signals, spurious signals or perturbations. According to its possible origins, two main categories exist:

- Environmental perturbations: Sky noise (e.g. the Sun, Milky Way,...), atmospheric noise (e.g. lightning discharges by thunderstorms,...), man-made noise (e.g. electric motors, arc welding, power lines,...)

- Crosstalk between systems (crosstalk noise): These are signals which are useful in one circuit, but unfortunately pass via parasitic coupling into nearby circuits, where they are undesired

Extrinsic noise is usually of a deterministic nature and therefore can not be treated statistically. Very often, the frequency of interfering signals is known in advance and results from the superposition of several deterministic signals.

2.4.2. Comparing Intrinsic and Extrinsic noise sources

Intrinsic noise shows up at the whole frequency band, rising towards lower frequencies due to the $1/f$ noise. Due to this wide frequency spectrum, it is very difficult to filter out intrinsic noise. Extrinsic noise on the other hand, usually has a very limited bandwidth, which makes it easier to avoid it by filtering. Another possibility is to shift the desired signal out of the extrinsic noise bandwidth.
The amplitude of intrinsic noise sources is rather low. For instance, a 100 kΩ resistance produces a thermal noise voltage of approximately 40 nV (rms) at room temperature ($T = 300$ K) and in the bandwidth of 1 Hz. Compared to that, interfering signals from industrial installations (e.g. power lines) reach the circuit of interest with higher amplitudes. It is difficult to predict the exact amplitudes and phases of those interferences, because they strongly depend on the coupling between noise source and victim. But in many cases the disturbances from external noise can have higher amplitudes as the investigated signal. Proper positioning of power and sensing lines, shielding of most sensitive parts and cables and appropriate grounding of the circuit board are some examples of actions limiting extrinsic noise. But it should always be kept in mind that, from an economic point of view, in the most cases reducing the emission of perturbations is more efficient than protecting the victims.
Calculating the noise levels of intrinsic noise is relatively easy compared to those of extrinsic noise sources. Several software packages exist to make intrinsic noise calculations, which deliver a fast and rough information of the noise produced in a circuit. Another way is to do the calculations by hand, which can be very cumbersome in many cases. Considering extrinsic noise, calculations are often much more complicated, because electromagnetic disturbances are described by Maxwell's equations. To solve these equations, complicated boundary conditions are necessary, which can be easily expressed in the time domain, but are almost impossible to formulate in the spatial

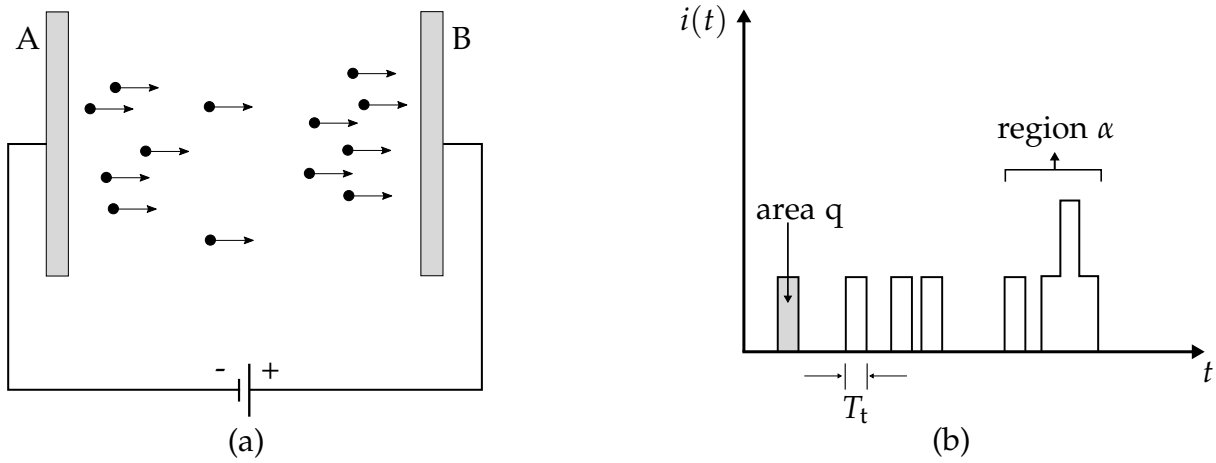

Figure 2.3.: (a) Electrons clustering in a vacuum tube, (b) elementary current pulses

domain. Therefore, it is easier to perform noise measurements to get an idea of the extrinsic noise levels.
In the following sections, the basic principles of intrinsic noise sources are presented.

2.4.3. Shot noise

The discrete nature of charge carriers is the physical origin of shot noise (also called Schottky noise). In a device with a potential barrier (e.g. a semiconductor), only the electrons with sufficient energy to pass the barrier contribute to the current through the device. When these electrons are crossing the potential barrier, they produce a series of independent, random events.
A stream of electrons in vacuum between the two electrodes A and B is shown in Fig. 2.3a. The electrons are emitted by electrode A and are collected by electrode B, which has a higher potential with respect to A. In every instant of time a different number of electrons is crossing a specific plane (e.g. plane B) in the vacuum tube. Reasons for that are the random emission rate of the electrons at plane A and the random distribution of electron velocities. Every electron will produce a current pulse in the external circuit, as depicted in Fig. 2.3b. The area of the current pulse is equal to the elementary charge q and T_t corresponds to the transit time an electron needs to cross the barrier. Region α shows a cluster of five electrons reaching plane B. From a microscopic perspective, the instantaneous current fluctuates about the mean, which is referred to as shot noise.
W. Schottky was the first to find the expression for shot noise in a vacuum diode [24]. The arrival of an electron at the collecting terminal is the elementary event in the classic

approach to estimate shot noise, which relies on Carson's theorem [25]. Neglecting the transit time T_t, the instantaneous current is the sum of elementary Dirac pulses of weight q

$$I(t) = q \sum_i \delta(t - t_i), \tag{2.2}$$

of which the mean value is

$$\overline{I}(t) = I_0 = \lambda q, \tag{2.3}$$

where λ is the average number of electrons collected per second. The (unilateral) *shot noise current spectral density* is

$$S_{\mathrm{sn}}(I) = 2qI_0, \tag{2.4}$$

and the shot noise is modeled as a noise current generator whose mean square value is

$$\overline{i_{\mathrm{sn}}^2}(t) = 2qI_0\Delta f, \tag{2.5}$$

where I_0 represents the average (DC) current flowing through the device.
As can be seen from Eq. (2.4) the frequency spectrum is obviously white, at least up to frequencies close to the reciprocal of the electron transit time. The instantaneous current amplitudes of shot noise are following a Gaussian distribution.
Shot noise is always generated in photomultipliers and all vacuum devices, as well as in junction diodes. In this case, the potential barrier is associated with the depletion zone of the pn junction.

2.4.4. Thermal noise

The physical origin of thermal noise is the thermal motion of free electrons in a conductive material. This motion is totally random which leads to spontaneous agglomeration of carriers at one end of the material or the other (as shown in Fig. 2.4a). Measuring the potential difference between the contacts A and B, a voltage as depicted in Fig. 2.4b will arise, which is called thermal noise voltage. The mean value of the fluctuating voltage V_{AB} must obviously be zero, as there is no reason that the charge carriers

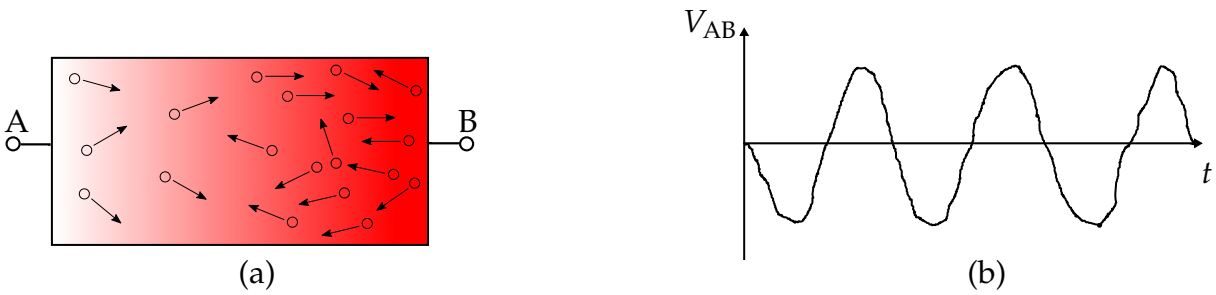

Figure 2.4.: (a) Spontaneous clustering of free electrons at contact B, (b) Course of the thermal noise voltage versus time

accumulate permanently at either terminal.
Nyquist's Theorem states that for linear resistances in thermal equilibrium, conduction mechanisms, the type of material as well as the shape and the geometry of the resistor do not affect the current or voltage fluctuations. Only the temperature and the value of the resistance have an influence on the generated noise. In the literature, four equivalent statements are encountered:

1. The *noise voltage spectral density*, under-open circuit condition, is a constant quantity, given by
$$S_{\text{tn}}(V) = \frac{\overline{v_{\text{tn}}^2}}{\Delta f} = 4k_B TR \tag{2.6}$$
2. The *noise current spectral density*, under short-circuit condition, is a constant quantity, given by
$$S_{\text{tn}}(I) = \frac{\overline{i_{\text{tn}}^2}}{\Delta f} = \frac{4k_B T}{R} \tag{2.7}$$
3. The *available noise power spectral density* (i.e., the noise power delivered to an identical resistor R, per unit bandwidth) is a constant quantity that depends solely on the temperature
$$S_{\text{tn}}(P) = k_B T \tag{2.8}$$
4. A noisy resistor is modeled by means of an identical noiseless resistor and a lumped external noise source (either a voltage - or current source). The equivalent circuits are shown in Fig. 2.5, where
$$\overline{v_{\text{tn}}^2} = 4k_B TR\Delta f \quad \text{(Thévenin model)} \tag{2.9}$$

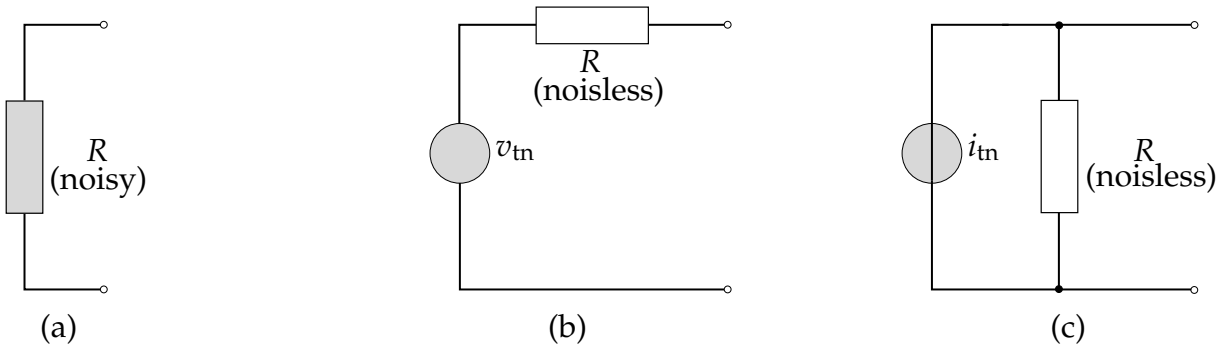

Figure 2.5.: (a) Noisy resistor, (b) Thévenin equivalent circuit, (c) Norton equivalent circuit

and

$$\overline{i_{tn}^2} = \frac{4k_B T \Delta f}{R} \quad \text{(Norton model)}. \tag{2.10}$$

As the Equations (2.6) and (2.7) show, the spectral density of thermal noise is constant with respect to frequency (property of white noise). Thermal noise is generated only in dissipative systems. For that reason it is associated with resistors and lightly doped semiconductor layers.

2.4.5. Diffusion noise

Carrier velocity fluctuations caused by collisions are the physical origin of diffusion noise. It is related to the diffusion process caused by a nonuniform carrier distribution. If the carrier density increases at one end of a semiconductor (for example by illumination), there is a natural tendency of the carriers to move towards regions with lower carrier density. This phenomenon is called diffusion. During this diffusion process the carriers are scattered by collisions with the lattice or impurity atoms, resulting in changed velocities. As the collisions happen completely random, also the diffusion current is random. A model for the diffusion noise was first introduced by Becking, followed by Van der Ziel [25]. In this model, they divided the volume of a semiconductor into elementary rectangular boxes ($\Delta x \cdot \Delta y \cdot \Delta z$). Random collisions of the electrons allow them to pass from one box to the next. These transitions are considered to be a series of independent events. The resulting current spectral density of the diffusion noise is given by

$$S_{dn}(I) = 4q^2 D_n n(x) \frac{\Delta y \Delta z}{\Delta x}, \tag{2.11}$$

where q is the elementary charge, $n(x)$ the electron concentration along the x axis, D_n the diffusion constant, and $\Delta x,\ \Delta y,\ \Delta z$ are the dimensions of the elementary box. With Einstein's relation

$$D_\mathrm{n} = \frac{k_\mathrm{B}T}{q}\mu_\mathrm{n} \tag{2.12}$$

(μ_n is the electron mobility), the current spectral density becomes

$$S_\mathrm{dn}(I) = \frac{4k_\mathrm{B}T}{\Delta R}, \tag{2.13}$$

with

$$\Delta R = \frac{\Delta x}{q\mu_\mathrm{n}n(x)\Delta y\Delta z}, \tag{2.14}$$

being the resistance of the elementary box.
By comparing Eq. (2.13) with Eq. (2.7) it can be seen that for majority carriers only, diffusion noise reduces to thermal noise. From a macroscopic point of view, the device's voltage-current characteristic has to be investigated: if it is linear (following Ohm's law), the noise is thermal; otherwise, it is diffusion noise. This can be illustrated taking a FET transistor as example: In the linear region it produces thermal noise, but as soon as the transistor is operated in the saturation region, it produces diffusion noise.

2.4.6. 1/f Noise (Flicker noise or Excess Noise)

The physical origin of $1/f$ noise is not completely understood up to now. One property of flicker noise is that it increases with decreasing frequency. It is also more prominent if electric currents are caused by very small numbers of charge carriers. Another property is that $1/f$ noise varies from sample to sample, even if they are designed identically. The level of noise depends on the fabrication quality of the device: high $1/f$ noise means poor quality and low reliability. Any inhomogeneity (in the lattice structure or materials) as well as contamination during processing or poor ohmic contacts can increase the flicker noise.
A possible explanation of the origin is that this kind of noise is a general process, which occurs in nonequilibrium systems (like the flow of a DC current through a device). Defects in the semiconductor lattice (including unwanted impurity atoms) as well as interactions between the charge carriers and surface energy states of the semiconductor may be reasons for the phenomenon of $1/f$ noise [26, 27].

Another source of $1/f$ noise may be imperfect contacts (e.g. between carbon granules in carbon resistors). This noise adds to the thermal noise of the resistor, which is the reason why it is also called "excess noise".
Many attempts have been made to model flicker noise. Bliek proposed a model in which the flicker noise is based on the diffusion equation [28], whereas Forbes suggests that the noise in semiconductor materials originates from localised high-frequency variations and long-range low-frequency fluctuations in the bulk [29].
In any case, $1/f$ noise can be modeled by a current generator, which has a mean square value of

$$\overline{i_{\mathrm{fn}}^2} = \frac{K\,I^{\alpha}}{f^{n}}\,\Delta f, \tag{2.15}$$

where K is a device-dependent constant and α is a constant that ranges from 0.5 to 2. For pink noise, characterised by constant power per octave, parameter $n = 1$ (although it may be 2 for fluctuations in the Earth's rotational speed, and $n = 2.7$ for galactic radiation). I represents the DC current flowing through the device.
In the model by Hooge [26, 27], flicker noise in homogeneous semiconductors can be characterised by a parameter α such that

$$\frac{S_{\mathrm{R}}}{R^2} = \frac{\alpha}{f\,N}, \tag{2.16}$$

with S_{R} being the power spectral density of the noise in the resistance, f the measurement frequency, and N the total number of free charge carriers. Therefore, α corresponds to the normalised contribution to the relative noise of a single electron, per unit bandwidth (it is assumed that the contributions of other electrons are independent). First, an average value of $2 \cdot 10^{-3}$ was proposed for α. Afterwards, it turned out that α also depends on the quality of the crystal. So in perfect materials α can be taken 2 or 3 orders of magnitudes lower.

2.4.7. Quantum noise

The fundamental origin of quantum noise is represented by the discrete nature of electromagnetic radiation. According to quantum mechanics, electromagnetic energy is absorbed or released in small discrete quantities, called photons. The energy of a photon can be calculated by

$$E = h\,f, \tag{2.17}$$

where $h = 6.63 \cdot 10^{-34}$ Js is Planck's constant and f corresponds to the frequency of its associated radiation. For a better understanding, consider an optical detector, which is exchanging energy (photons) with its environment. The flow of the energy between the detector and the environment has a fluctuation which is evoked by the random number of photons radiated or absorbed per second. This phenomenon is called quantum noise.
Quantum noise can be neglected up to frequencies of about 10^{15} Hz. In that spectral range, the thermal noise looses its importance and, therefore, quantum noise begins to play a role. It is also relevant at very low temperatures (several Kelvins), where the thermal noise is also less significant.

2.4.8. Generation-Recombination Noise (G-R Noise)

G-R noise is related to fluctuations in the population of charge carriers, due to random generation, random recombination, random trapping and the release of carriers in a semiconductor. Generation takes place, when an electron-hole pair is broken. To brake a covalent bond, an uptake of energy is needed. The energy can be supplied by photons, which are of discrete, nonuniform nature. That means, that the generation of charge carriers is a random process, both in space and in time.
Pair recombination is the opposing process to charge generation. It takes place every time an electron meets a hole. The Brownian motion of the carriers is the reason for that encounter, and thus recombination also has random nature.
Trapping of electrons and holes by impurity atoms can also have an effect on the magnitude of G-R noise. This process induces additional fluctuations in the population of charge carriers. All crystal lattice defects act as so-called traps.
In general G-R noise has no great impact in semiconductors with common doping levels, because the charge carriers introduced by the dopant dominate those who are generated by thermal or optical processes. This kind of noise shows an effect if carrier concentrations are relatively low, like in intrinsic semiconductors, lightly doped semiconductors and in the space charge layer of every junction.

2.4.9. Popcorn (Burst) noise

The physical origin of burst noise is not completely understood, but it seems it has to do with heavily doped emitter junctions. It is observed in many planar-diffused devices, like tunnel diodes, bipolar transistors, integrated circuits, film resistors and so on. Contamination by heavy metallic atoms during processing or damages to the crystal lattice close to the junctions are thought to be the onset of this noise [25]. The appearance and disappearance of bursts is associated with single-trap activity in regions with few free carriers (like the depletion region of the emitter junction).
Some properties of popcorn noise are:

- Bursts show up at random rates
- The noise spectrum is proportional to $1/f^2$
- The amplitude of popcorn noise is typically 2 to 100 times that of thermal noise
- It may affect only a few samples out of a fabricated series, which implies poor quality

Due to progress in manufacturing technologies, burst noise plays only a minor role nowadays.

2.4.10. Avalanche noise

Avalanche noise has its origin in the process of carrier multiplication due to impact ionisation in reverse biased p-n junctions. The electric field inside the depletion zone is augmented by an increasing reverse bias voltage. This leads to an enhanced acceleration of the minority carriers in the p-n junction (holes in the n region and electrons in the p region). When they collide with neutral atoms of the lattice, they can generate additional electron-hole pairs. This newly generated carriers are further accelerated and lead to more and more collisions, which again produce new electron-hole pairs. If there are imperfections in the crystal lattice, a kind of microplasma is formed and the current through the junction is increased dramatically. A breakdown of the device occurs, if this avalanche process cannot be controlled. The spectrum of avalanche noise is white and it mainly affects reverse-biased diodes operated at more than 8 V.

2.4.11. Noise in different components

The different noise mechanisms which were discussed in the prior subsections are present in electronic elements to a greater or lesser extent. This depends mainly on their structure, bias, temperature, operating frequency and so forth. Table 2.1 gives an overview of different components and their corresponding noise under varying operating frequencies.

Table 2.1.: Noise in various electronic components depending on operating frequency

	Zero bias	Low frequency (with bias)	High frequency (with bias)	$f > 1$ THz
Resistor	thermal	1/f	thermal	thermal quantum
Diode	thermal	shot 1/f G/R avalanche	shot	
Bipolar Transistor	thermal	shot 1/f G/R popcorn	thermal shot	
FET	thermal	thermal diffusion shot G/R	thermal diffusion	
MOS	thermal	1/f thermal diffusion		

3. Methods

3.1. Photodetection readout circuit

3.1.1. Basic functionality

The main part of the electronic circuit used for the measurement of the photocurrent I_p is shown in the diagram in Fig. 3.1. Originally, it was utilised to measure photocurrents of phototransistors (PhTrs)[30]. In general, the current levels of PhTrs are decades higher than those of photodiodes. Since a PD is used to measure the light flux through the MEMS structure, the first task of this thesis was to optimise the photodetection circuitry for the measurement of photocurrents in the range of 10^{-11} A to 10^{-7} A.
The operational amplifier (OPAMP) in Fig. 3.1 is part of an OPA404KP quad operational amplifier (consisting of four individual OPAMPs) and the operating voltage of the circuit is set to ± 12 V. As shown in the circuit diagram, the PD is used in a reverse bias configuration. As a consequence, the relationship between incident optical power and the photocurrent is linear over a wide range [31]. By choosing the two resistors $R_1 = 20$ kΩ and $R_2 = 10$ kΩ in a voltage divider configuration, the reverse bias voltage is set to 4 V used for the inorganic PD. In a later stage of the thesis, organic PDs are utilised to detect the light flux and thus the reverse bias has to be changed to 1.5 V ($R_1 = 70$ kΩ and $R_2 = 10$ kΩ). Higher reverse bias would harm the organic material of the OPD and reduce its lifetime.
The resistor R_s and the potentiometer R_{comp} compensate a possibly existing offset voltage at the output of the OPAMP. For the use with the inorganic PD, R_s is chosen with 10 kΩ, whereas it has to be changed to 5 MΩ when the organic PD is employed as detector, due to the modified reverse bias. In Sec. 3.1.3 the correct adjustment of the potentiometer is explained.
The feedback resistor R_f defines the amplification factor of the photocurrent I_p. In principle, the OPAMP with the resistor R_f in the negative feedback branch works as a

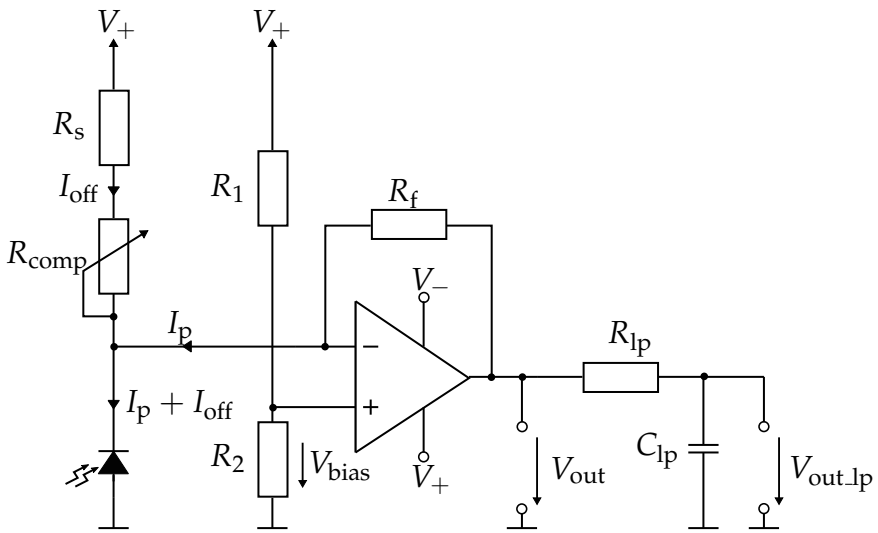

Figure 3.1.: Readout circuit of the MEMS sensor with the PD which is detecting changes in the light flux induced by vibrations, resulting in a proportional photocurrent I_p. Origin of the offset current I_{off} is the current generated in the sensor's resting position. It is compensated by the correct adjustment of the potentiometer R_{comp}.

transimpedance amplifier (TIA), which produces a voltage

$$V_{out} = I_p R_f \tag{3.1}$$

at the output of the TIA. Taking all the resistors and the potentiometer for offset compensation into account, the voltage at the output of the TIA arises to

$$V_{out} = V_+ \frac{R_2}{R_1 + R_2} \left(1 + \frac{R_f}{R_s + R_{comp}}\right) - V_+ \frac{R_f}{R_s + R_{comp}} + I_p R_f, \tag{3.2}$$

where V_+ is the positive supply voltage for the circuit. The output of the TIA is followed by a RC low-pass (corner frequency $f_c = 10.6$ kHz), consisting of the resistor R_{lp} and the capacitor C_{lp}. Alternatively, the output can be used also without the low-pass. An LED is used as the light source of the vibration sensor. The current driving the LED is controlled by a constant current source comprising another OPAMP of the OPA404KP and a potentiometer, among other elements (this part of the circuit is not shown in Fig. 3.1). By adjusting the resistance of the potentiometer, the current through the LED can be set. In an usual experiment the LED current is set to $I_{LED} = 4$ mA.

3.1.2. Improving the SNR

In the old detection circuit, a feedback resistor R_f =10 kΩ was used. For the new detection circuit intended to measure PD currents, this resistor was increased to 1 MΩ, because the lower currents produced by the PD (compared to the PhTr) need larger amplification to deliver a good-quality signal. Also the signal to noise ratio (SNR) of the output voltage is improved by increasing the feedback resistance, assuming that only the thermal noise voltage ($\propto \sqrt{R_f}$) is significant (see Subsec. 2.4.4). According to Eq. (2.1), a higher resistance also leads to a higher thermal noise voltage. By increasing the feedback resistance R_f of the TIA in the detection circuit by a factor $\beta = 100$, the according thermal noise voltage v_{tn} will rise by $\sqrt{\beta}$. At the same time the output signal V_{out} of the TIA will increase according to Eq. (3.1) by β. Consequently, the SNR will improve by $\beta/\sqrt{\beta} = \sqrt{\beta} = 10 = 20$ dB.
Another opportunity to improve the SNR of the readout circuit can be identified when having a closer look on the shot noise current produced by the PD. It is derived from Eq. (2.5) with

$$i_{snPD} = \sqrt{2qI_p\Delta f}. \tag{3.3}$$

The equation shows, that i_{snPD} rises proportional to $\sqrt{I_p}$. If the detectable optical power of the PD is increased, the photocurrent I_p rises proportional to it. Therefore, the detectable optical power should be as large as possible [31], because the SNR will be increased by $I_p/i_{snPD} = I_p/\sqrt{I_p} = \sqrt{I_p}$.
In the case of the MEMS vibration sensor, increasing the detectable optical power of the PD can be achieved by increasing I_{LED} through the LED which acts as the light source of the sensor package. The maximum forward current of the inorganic green LED in use is given by the data sheet with $I_{max} = 20$ mA. But for reasons of OLED lifetime, I_{LED} was kept at 4 mA. Another possibility to optimise the detectable optical power is to perfectly align the sensitive area of the PD with the optical window of the MEMS sensor and the emitting area of the LED (explained in Sec. 3.2).
Additionally, it is advantageous to limit the bandwidth of the circuit, because this will lead to both a lower thermal noise voltage and shot noise current (according to Eq. (3.3) and subsections 2.4.3 and 2.4.4). The corner frequency of the low-pass is defined by

$$f_c = \frac{1}{2\pi R_{lp} C_{lp}}. \tag{3.4}$$

For $R_{\mathrm{lp}} = 1500\ \Omega$ and $C_{\mathrm{lp}} = 10$ nF, a corner frequency of 10.6 kHz is achieved (compared to 106 kHz in the old detection circuit), which will not influence the measurements in the frequency range of interest (up to 2 kHz) and will damp all frequencies higher than f_{c}.
The original detection circuit contained an optional additional amplifier stage, which was built out of an OPAMP in an inverting amplifier configuration, augmenting the output of the TIA by a factor of -10. In the new detection circuit, this additional amplification was not necessary since the TIA amplifies the photocurrent already by a factor of 10^6 V/A. In addition, the second amplification stage introduced noise. Therefore, omitting the second amplification stage results in an improvement of the SNR, too.

3.1.3. Offset compensation (Simulation in QUCS)

For optimal operation of the sensor, no DC voltage should be generated at the output, but only an AC component. This AC voltage signal corresponds to the AC component of the photocurrent I_{p} induced by the oscillations of the MEMS inertial mass. For the application as vibration sensor, this is the quantity of interest. The DC component originates from the current which is induced in the resting position of the sensor (see Sec. 3.2). It is normally in the range of 10^{-7} A. Via the feedback resistance R_{f} of the TIA this current results in an unwanted offset in the output voltage. By adjusting the resistance of R_{comp} it is possible to eliminate this offset. Therefore, the maximum value of the potentiometer has to be in the right resistance range. Otherwise, changing the resistance will never lead to a compensated output and in the worst case will saturate the output of the OPAMP.
The value for the potentiometer R_{comp} to compensate the offset can be calculated in a first step by setting V_{out} and the photocurrent I_{p} in Eq. (3.2) to zero, leading to

$$R_{\mathrm{comp}} = \frac{R_{\mathrm{f}} R_1}{R_2} - R_{\mathrm{s}}. \tag{3.5}$$

With the standard values for the resistors described above, the maximum value of the offset compensation potentiometer is 1.99 MΩ. If a DC offset current I_{off} is considered in the calculation of R_{comp} the value of the potentiometer changes according to

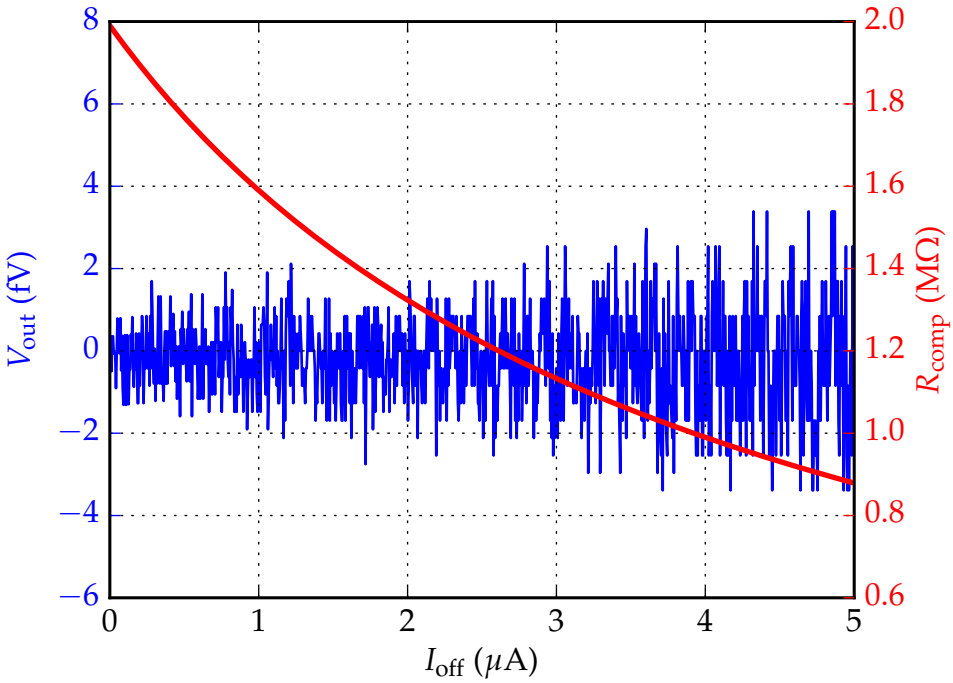

Figure 3.2.: R_{comp} and the voltage V_{out} at the output of the TIA in dependence of a rising DC offset current. By adjusting the potentiometer, the output can be compensated.

$$R_{comp} = \frac{R_f R_1}{R_2 + (R_1 + R_2)\frac{I_{off} R_f}{V_+}} - R_s. \tag{3.6}$$

The software QUCS is used to simulate the readout circuit. The intention of this simulation is to watch the resistance change of the compensation potentiometer R_{comp} and the corresponding output voltage at the TIA, if I_{off} is changing. Calculation of R_{comp} is done according to Eq. (3.6). In the simulation circuit, an ideal DC current source (swept from 1 nA to 5 µA via a DC simulation sweep) replaces the PD to imitate the DC offset photocurrent. All resistances, the capacitances and the voltage sources are according to the real readout circuit. The results of the simulation are plotted in Fig. 3.2, in which the resistance of R_{comp} is depicted in red and the offset voltage at the TIA output V_{out} in blue. It is shown that the value of R_{comp} decreases from 1.99 MΩ with increasing I_{off}. For the ideal OPAMP in the simulation, the output voltage is kept in the range of several femtovolts, though it is clear that these voltage values will not be those measured at the real circuit output. Nonetheless, the simulation illustrates the offset compensation quite well.

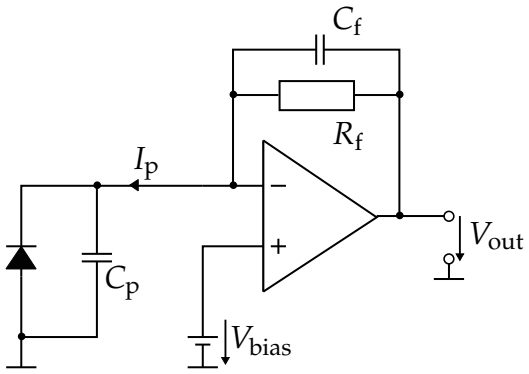

Figure 3.3.: A TIA with a reverse biased PD at the inverting input and the capacitor C_p, representing diode capacitance and input capacitance of the OPAMP. C_f prevents oscillations of the output.

3.1.4. TIA bandwidth

The transimpedance amplifier is a standard OPAMP circuit which is used to measure low-level currents such as currents generated by photodiodes. Compared to other PD readout circuits (PD with high impedance load resistor or a voltage follower configuration), this kind of OPAMP configuration has several advantages, e.g. a high amplification factor of the photocurrent accompanied with a large bandwidth [31]. A schematic of a TIA connected to a reverse biased PD (like in the readout circuit used) is shown in Fig. 3.3. Herein C_p represents the sum of the parasitic capacitance of the PD and the input capacitance of the OPAMP, whereas C_f corresponds to the feedback capacitance needed to stabilise the circuit (for more on that see Subsec. 3.1.5).
In the readout circuit used a reverse bias of $V_{bias} = 4$ V (in the case of the inorganic PD) is applied at the non inverting input of the OPAMP, realised by a voltage divider (resistances R_1 and R_2). By increasing the reverse bias of the PD, the parasitic capacitance is lowered, which enhances the bandwidth of the circuit. The bandwidth is given by

$$\Delta f = \sqrt{\frac{GBW}{2\pi R_f C_p}}, \tag{3.7}$$

in which GBW is the gain bandwidth product of the OPAMP. The gain bandwidth product of the OPA404KP is given with $GBW = 6.4$ MHz in the data sheet and the PD has an internal capacitance of $C_D = 730$ pF at $V_{bias} = 3$ V. Calculating the bandwidth of the TIA with these values and a feedback resistor $R_f = 1$ MΩ leads to

$$\Delta f = \sqrt{\frac{6.4\ \text{MHz}}{2\pi \cdot 1\ \text{M}\Omega \cdot 730\ \text{pF}}} = 37.35\ \text{kHz}. \tag{3.8}$$

This calculation shows that the bandwidth of the TIA is sufficient for the readout of the MEMS modulated photocurrent, which will be a signal with a maximum frequency in the range of several kHz. It is obvious that the bandwidth calculated in Eq. (3.8) is not the true value of the readout circuits bandwidth (because of different PD capacitance due to $V_{\text{bias}} = 4$ V, additional capacitances of the OPAMP and circuit lines), but it is a good estimation. Furthermore, the bandwidth of the circuit is limited by the RC low-pass at the output to 10.6 kHz (see Sec. 3.1.1), which allows for increasing R_{f} even further.

3.1.5. TIA stabilisation

TIAs often show a tendency to an oscillating output voltage, usually at a frequency around its unity gain frequency. The reason for that is the additional phase shift of the $R_{\text{f}}C_{\text{p}}$ low-pass, which adds to the amplifiers internal phase shift. At some frequency this can lead to a positive feedback of the TIA. If the gain of the circuit is above unity, the whole circuit starts to resonate [31]. One possibility to stabilise the output is to implement a capacitance C_{f} in parallel to R_{f}. Measurements with the old readout circuit showed that the circuit output voltage V_{out} shows exactly this oscillations, if the capacitance is not implemented.
Finding the optimal value of this feedback capacitance can be tricky and several approaches exist to find it. Generally, the value of C_{f} will be in the range of several picofarads (pF). One of the approaches is just trial and error, another one is outlined in the application report SBOA055A by Texas Instruments [32]. Therein, Eq. (3.9) for the calculation of C_{f} is derived from the noise gain (i.e., the noninverting closed-loop gain) of the TIA, which determines the stability of the circuit.

$$C_{\text{f}} = \frac{1}{4\pi R_{\text{f}}\ GBW}\left[1 + \sqrt{1 + 8\pi R_{\text{f}} C_{\text{p}}\ GBW}\right] \tag{3.9}$$

Pasting the values of R_{f}, GBW and C_{p} from above, will give a theoretical feedback capacitance $C_{\text{f}} = 4.27$ pF, which should be placed in parallel to R_{f} in order to prevent an oscillation of the output voltage V_{out}. An AC simulation in QUCS is performed to show the effect of different values of C_{f} on the circuits output voltage V_{out}. A schematic

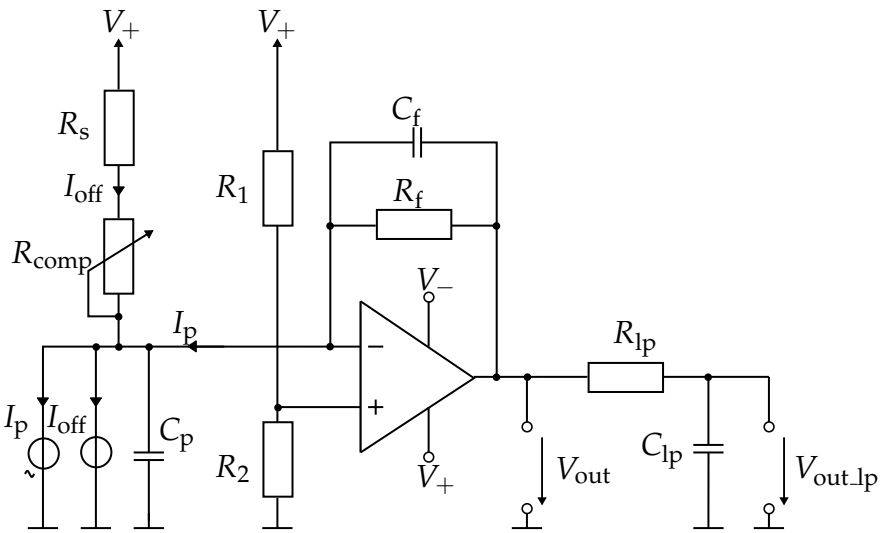

Figure 3.4.: QUCS simulation circuit to see the effect of a changing feedback capacitance C_f in an AC simulation. The DC current source I_{off}, the AC current source I_p and the capacitance C_p are taking over the functionality of the photodiode.

of the simulation circuit is depicted in Fig. 3.4.

Compared to the simulation circuit of the offset compensation, some minor changes are necessary for the AC simulation. The type of the OPAMP used is changed from the standard OPAMP to the OPA27 from Texas Instruments, because its model is a more realistic one (an OPA404KP is not available in the QUCS library). In parallel to the DC current source (I_{off} = 0.2 µA), an AC current source (I_p = 1 µA) is used to simulate the modulated photocurrent from the MEMS structure. The capacitance C_p in parallel to the current sources represents the parasitic capacitance of the PD and the feedback capacitance C_f is added to demonstrate the stabilisation effect. Choosing $C_p = 480$ pF leads to a simulation result which fits quite good to the measurement data of Sec. 4.2, as will be seen later. An AC simulation from 1 Hz to 100 kHz is conducted and the results for three different values of C_f (4.27 pF, 0.2 pF and without C_f) are plotted in Fig. 3.5. The simulation data show, that an increasing feedback capacitance leads to a stable and flat frequency response.

Contrary to this simulation, no such oscillations were observed in the new readout circuit. Even without a feedback capacitance there is no oscillation of V_{out} at all. This could be explained by the parasitic capacitance of R_f and capacitances of circuit lines, which seem to be sufficiently high to stabilise the circuit. In Sec. 4.2, noise voltage measurement data of the readout circuit are presented which show the noise gain behaviour of the circuit (noise peaking, see figures 4.3 and 4.4). Apparently, the noise

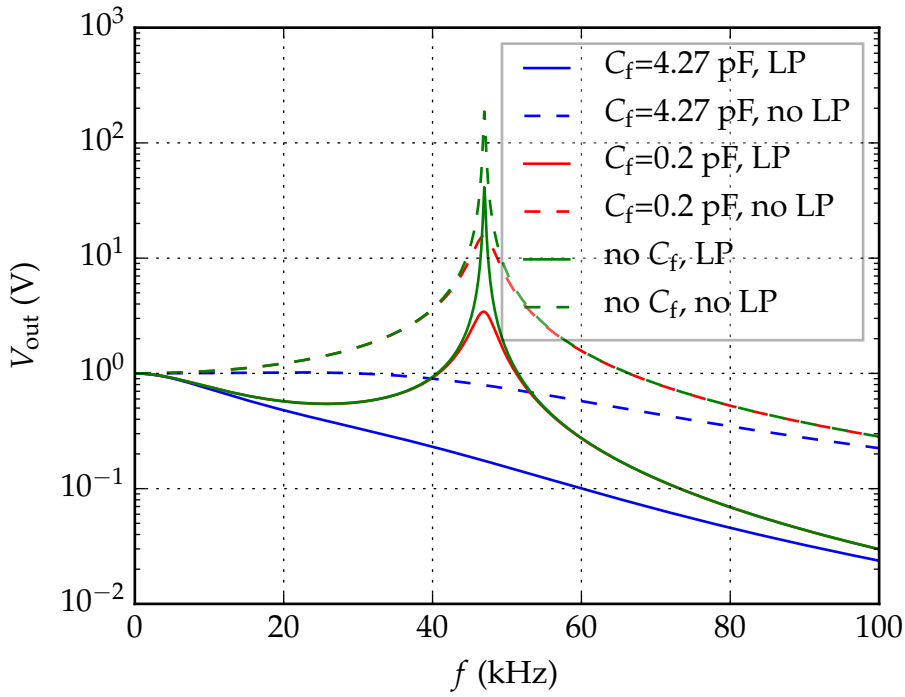

Figure 3.5.: V_{out} of the AC simulation with different values of C_f and the effect of low-pass filtering. Increasing the feedback capacitance C_f stabilises the output. Solid lines depict the output of the TIA after the low-pass filter with a corner frequency of $f_c = 10.6$ kHz, whereas the dotted lines present the output voltage in front of it. For the calculated value of $C_f = 4.27$ pF, the blue curves show the optimal courses of V_{out}.

gain is in a range, where it does not cause an oscillation of the output.

3.2. The MEMS Sensor

3.2.1. MEMS Sensor principle

The basic principle of the sensor has already been described in several works and articles [8, 16, 33] but will be outlined here for the sake of clarity. The MEMS vibration sensor in general comprises four layers on top of each other. To get a better idea, one can consider the vertical structure of the sensor sandwich-like (see Fig. 3.6). A light source (LED or OLED) serves as the top layer, whereas the bottom layer of the sensor consists of a light detection element (PD or OPD). As of now, these two layers are no permanent components of the MEMS sensor, but fixed by adhesive tape (in case of using OLED and OPD) or a special plastic chip holder (in case of using LED and PD) to the MEMS structure. Two grids laying on top of each other are placed between these two layers. One of these grids can move horizontally with respect to the other one. The upper grid consists of a glass chip, on which a chromium pattern is vapour-deposited. This layer is fixed via SU-8 bonding to the frame of a silicon on insulator (SOI) chip. The frame serves as the anchor point for the four u-shaped springs, which bear the moveable Si mass (the second grating). A deep reactive ion etching (DRIE) process is used to manufacture the grid (2 mm $\times$ 2 mm in size) of the oscillator with rectangular holes in the µm range. A rotation or translation in y- or z-direction of the structure is impeded by the special u-shape of the springs, hence only movement in the horizontal x-direction is possible.
In operation, the LED is driven by a DC current and produces light which travels through the glass chip and reaches the chromium grid pattern. The portion of the light passing the first grid hits the Si oscillator. Depending on the position of this moveable spring-suspended grating, a higher or lower percentage of the incoming light is able to pass through the holes. The position of the moveable mass is directly influenced by vibrations acting on the Si frame. These vibrations can have various origins like earthquakes, driving cars, public transport, rotation, etc. But also activities of the human body (e.g. respiration and heart contractions) can induce a change in position of the Si grating. In the position where the holes of the moveable mass lie directly beneath the holes in the chromium pattern, a maximum amount of light passes the

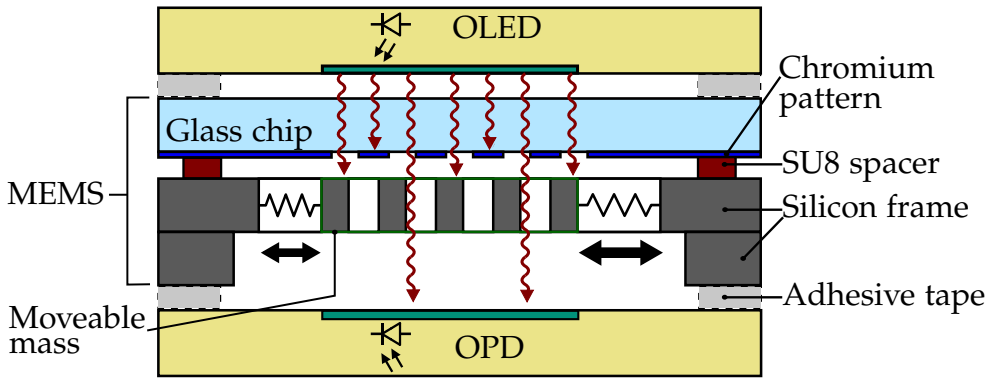

Figure 3.6.: Cross section of a MEMS vibration sensor with organic optical readout [16].

second grating and reaches finally the PD. There, the optical power is converted into an electric current. Considering the opposite case, if the holes in the silicon oscillator are located directly beneath the opaque chromium pattern, no light can pass the second grating and therefore no light from the LED reaches the PD. The current produced by the PD is not zero in this case, but the minimum value, which can be explained by the dark current inherent to every PD. By the detection circuit used in this work, this dark current can be compensated.

As up to now, inorganic semiconductors have been used in the vibration sensor setup. During this work the setup is transferred to the use of organic semiconductors. This should lead to a higher compactness of the sensor and a more homogeneous distribution of the light source, due to the advantages of the organic components. Sensitivity measurements were conducted with both setups and the results are presented in Sec. 4.3. By depositing a Cr grid directly on the glass cover of the OLED or OPD, the glass chip of the MEMS with the Cr grid could be omitted, which would further reduce the sensor size. Sec. 4.5 reveals the measurement results of such a sensor setup.

3.2.2. Mathematical model of the mechanical response

In order to describe the mechanical response of the sensor in a mathematical model, it is first important to get an overview of the parameters which influence the mechanical behaviour of the MEMS. Therefore, a schematic of the MEMS in case of using it as vibration sensor is designed and depicted in Fig. 3.7a [16]. A vibration in the form of a periodical actuation $x_a(t) = X_0\, e^{i\omega t}$ (X_0 being the vibration amplitude and ω the angular frequency of the vibration) deflects the frame of the MEMS sensor. Via

the suspension, which can be described by a spring-damper system, the actuation is transferred onto the mobile mass. The mechanical response of the sensor to the actuation $x_\mathrm{a}(t)$ is the differential deflection $x_\mathrm{d} = x_\mathrm{m} - x_\mathrm{a}$, in which x_m corresponds to the displacement of the mobile MEMS part with mass m and x_a corresponds to the displacement of the sensors frame, the deflection of the chromium grid pattern respectively.
This mechanical setup is identical with a driven damped oscillator [34] and is described by the equation of motion

$$m\ddot{x}_\mathrm{d} + d\dot{x}_\mathrm{d} + kx_\mathrm{d} = F\mathrm{e}^{\mathrm{i}\omega t}, \tag{3.10}$$

with k being the stiffness of the spring, d the damping factor and m the mass of the mobile grid. The right part, $F\mathrm{e}^{\mathrm{i}\omega t}$, describes the external force acting on the frame.
Introducing the decay parameter $\gamma = d/2m$ and the (angular) natural frequency $\omega_0 = \sqrt{k/m}$ leads to

$$\ddot{x}_\mathrm{d} + 2\gamma\dot{x}_\mathrm{d} + {\omega_0}^2 x_\mathrm{d} = \frac{F}{m}\mathrm{e}^{\mathrm{i}\omega t}, \tag{3.11}$$

by dividing Eq. (3.10) by the mass m.
The right hand side of Eq. (3.11), $F/m\ \mathrm{e}^{\mathrm{i}\omega t}$, is equal to a periodical acceleration and can therefore also be written as the second derivative of the deflection $x_\mathrm{a}(t)$ which is given by $-X_0\omega^2\mathrm{e}^{\mathrm{i}\omega t}$. Solving this ordinary second order inhomogeneous differential equation can be done by making a complex ansatz

$$\ddot{z} + 2\gamma\dot{z} + {\omega_0}^2 z = -X_0\omega^2\mathrm{e}^{\mathrm{i}\omega t} \qquad \text{with } z = x + \mathrm{i}y. \tag{3.12}$$

The general solution of Eq. (3.12) consists of a transient and a stationary part. For sufficiently long times $t \gg 1/\gamma$ (which is true for the vibration MEMS sensor with periodic actuation), the amplitude $A\mathrm{e}^{-\gamma t}$ of the transient part decreases into a range where it can be neglected. Only the stationary part with an oscillation frequency enforced by the angular frequency ω of the external actuation remains. This part results from finding the particular solution of the differential equation. It is easily achieved by setting $z = A\mathrm{e}^{\mathrm{i}\omega t}$ and use it in Eq. (3.12) which will lead to the frequency dependent amplitude function

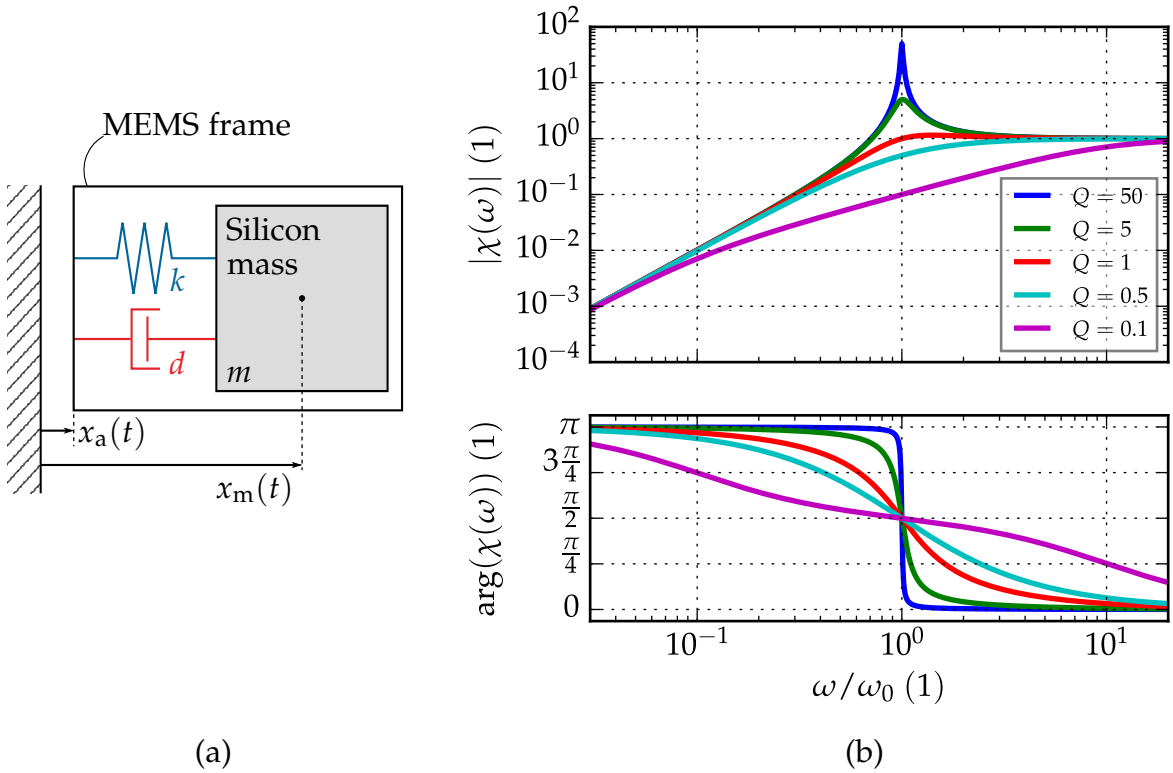

Figure 3.7.: (a) Lumped parameter model of the MEMS vibration sensor [16]. (b) Magnitude (top) and phase (bottom) of the sensor's transfer function, also called Bode plot, with different values of the quality factor Q.

$$A(\omega) = \frac{X_0 \omega^2}{\omega^2 - {\omega_0}^2 - 2\mathrm{i}\gamma\omega}. \tag{3.13}$$

Dividing $A(\omega)$ by the excitation amplitude of the MEMS sensor X_0 delivers the transfer function

$$\chi(\omega) = \frac{\omega^2}{\omega^2 - {\omega_0}^2 - 2\mathrm{i}\gamma\omega}. \tag{3.14}$$

Fig. 3.7b shows the magnitude and the phase of the vibration sensor's mechanical response for different values of the quality factor Q. The quality factor indicates the height of the magnitude at the resonance frequency ω_r. For $\gamma \ll \omega_0$ the resonance frequency is more or less equal to the natural frequency and Q is given by

$$Q = |\chi(\omega_0)| = \frac{\omega_0}{2\gamma} = \frac{\sqrt{km}}{d}. \tag{3.15}$$

The quality factor is the central parameter of any kind of oscillator (mechanical, electrical, etc.) and is defined as the ratio of stored energy to dissipated energy in one oscillation cycle. A small damping factor d leads to high Q which has the effect of a high and sharp resonance peak in the magnitude function, whereas high d means low Q and a reduced and broadened peak. In the case of overdamping ($Q < 0.5$) even no peak is feasible (degenerated peak).
Below the eigenfrequency $(\omega < \omega_0)$, the magnitude function increases proportional to ω^2, because $|\chi(\omega < \omega_0)| \approx \omega^2/\omega_0^2$, whereas at an actuation frequency higher than the resonance $(\omega > \omega_0)$, the magnitude is equal to one according to $|\chi(\omega > \omega_0)| \approx 1$.
Apparently, for systems with high Q the phase information in Fig. 3.7b changes from $+\pi$ to 0 at the natural frequency ω_0. High Q leads to a sharp and steep phase turn, whilst the effect of a low Q value is a slow and smooth change of phase. All curves run through $\pi/2$ at ω_0, whatever Q-factor.

3.2.3. Sensitivity

Sensitivities of transducers in general are defined as the proportion between the change of the output signal with respect to the input quantity. Considering the MEMS vibration sensor, the output quantity is the output voltage of the TIA, V_{out}, whereas the input quantity is the differential deflection of the sensor x_{d}. This leads to the total sensitivity $S = \delta V_{\text{out}}/\delta x_{\text{d}}$ of the vibration sensor. The transduction described by S consists of several transduction steps, each specifying the relation between two physical quantities, e.g. the light flux Φ passing through the two grids of the sensor obviously depends on the open area A_{open} [16].
Fig. 3.8 shows how A_{open} is related to the displacement of the stationary grid with respect to the moving Si mass. The holes of the grids are of rectangular shape, which means that the light flux depends linearly on the deflection of the oscillating mass. Other hole shapes would be technically possible, but would change the linear dependency between displacement and light flux, which could be preferable in special cases [35]. Width w_{h} and length l_{h} of the holes are in the range of µm, e.g. 20 µm and 100 µm, respectively.
The spacing d_{h} in x-direction between the holes needs to be at least w_{h}, otherwise the light flux would not be proportional to the deflection either (an overlap with the adjacent hole would occur). Due to alignment errors during early fabrication, the holes

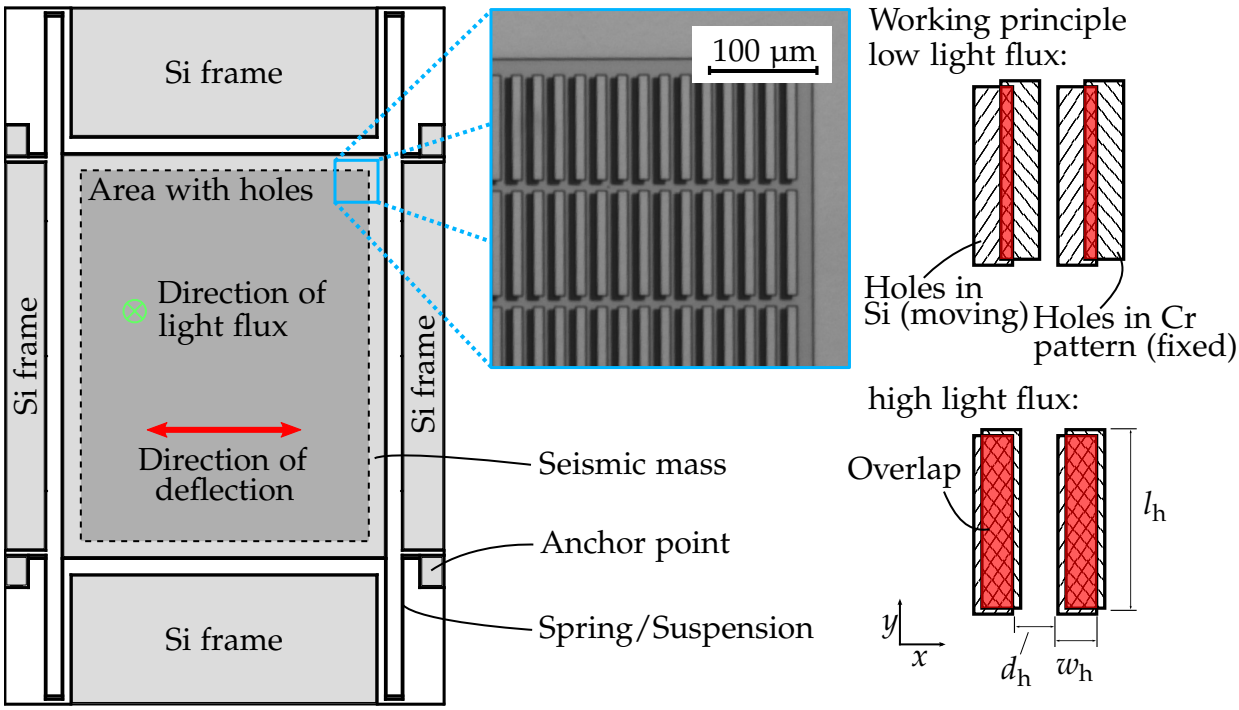

Figure 3.8.: Top view of the MEMS sensor. The seismic mass in the centre of the sensor is suspended by four u-shaped springs. The micrograph shows the arrangement of holes in detail. On the right, the working principle of the sensor is depicted, showing two different cases of possible hole positions. Low light flux: The overlap of the holes in the Si seismic mass and the Chromium pattern is small. Light can pass only through a very narrow slit, depicted in red colour. High light flux: The two holes overlap almost completely. The light flux is close to the maximum [16].

in the Cr pattern and in the Si mass are shifted in y-direction in Fig. 3.8. But since the manufacturing process has improved and thus, the offset has almost vanished, it can be neglected. The resting position of the moveable mass is defined by the alignment in x-direction. It is perfect, if $A_{\text{open}} = A_{\text{max}}/2$, which means that a pair of holes is overlapping with half of their area. The maximum possible deflection x_{d} would then be $w_{\text{h}}/2$ in both directions and the resulting area A_{open} would alternate between 0 and $A_{\text{max}} = w_{\text{h}} l_{\text{h}}$.
Spacing and dimension of the holes determine the number of holes N_{h} a structure of size 2×2 mm^2 can bear. So the total change in the translucent area δA_{open} can be calculated by

$$\delta A_{\text{open}} = N_{\text{h}} l_{\text{h}} \delta x_{\text{d}} = \alpha_1 \delta x_{\text{d}}. \tag{3.16}$$

A change in the open area leads to an alteration in the light flux $\delta\Phi = \alpha_2 \delta A_{\text{open}} = (1-r) E_{\text{e}} \delta A_{\text{open}}$. The term $(1-r)$ originates from reflective losses when the light from the LED passes through the glass chip and E_{e} is the energetic irradiance of the LED. In a next step, the altered light flux implies a variation in the photocurrent $\delta I_{\text{p}} = \alpha_3 \delta\Phi = \eta_{\text{q}} e \delta\Phi$, with η_{q} being the quantum efficiency of the photodiode and e the electron charge. Finally, the electronic readout circuit converts δI_{p} to a change in the output voltage $\delta V_{\text{out}} = \alpha_4 \delta I_{\text{p}} = R_{\text{f}} \delta I_{\text{p}}$. The total sensitivity is calculated by multiplication of all partial sensitivities, yielding

$$S = \frac{\delta V_{\text{out}}}{\delta x_{\text{d}}} = \prod_{\text{i}=1}^{4} \alpha_{\text{i}} = \frac{\delta V_{\text{out}}}{\delta I_{\text{p}}} \frac{\delta I_{\text{p}}}{\delta \Phi} \frac{\delta \Phi}{\delta A_{\text{open}}} \frac{\delta A_{\text{open}}}{\delta x_{\text{d}}} = R_{\text{f}} \eta_{\text{q}} e (1-r) E_{\text{e}} N_{\text{h}} l_{\text{h}}. \tag{3.17}$$

As the result of Eq. (3.17) suggests, several parameters can be tuned to enhance the sensitivity of the MEMS sensor. First of all, with increasing effective edge length $l_{\text{e}} = N_{\text{h}} l_{\text{h}}$, the sensitivity is raised. This intrinsic sensor parameter is limited by the size of the moveable mass. Increasing the number of holes N_{h} would mean that they have to be placed closer together. Therefore, the distance d_{h} between the holes has to be reduced or the width of the windows has to get smaller. This facts limit the maximum number of holes, because the maximum deflection is reduced, which means a loss in dynamic range.
Extrinsic parameters which influence the sensitivity are the feedback resistance R_{f} of the amplifier circuit and the irradiance E_{e} of the LED. It is not possible to increase the resistance without any limits, because according to Eq. (3.7) it narrows the bandwidth

of the TIA. The irradiance could be improved by simply choosing a higher current running through the light source, with the drawbacks of a higher power consumption and an accelerated decay of the OLED material. Also the reflective losses $(1 - r)$ of the glass chip could be minimised and a PD with higher quantum efficiency η_q could be chosen to get a better sensitivity, but this two parameters have very little impact on the overall output [16].

3.3. Measurement setup

Different types of measurements were carried out within the scope of this diploma thesis. First of all, the characteristic transfer functions of several MEMS sensors were measured to compare the performance of the newly designed readout circuit with the original readout circuit (using a phototransistor). A laser-Doppler vibrometer (LDV) is measuring the displacement of the MEMS frame, as already applied successfully within other works [8, 16, 30]. The noise performance of the circuits was also compared by noise measurements executed with a SR780 Network Analyzer.
Furthermore, measurements of MEMS sensor's transfer functions using organic LEDs and PDs were performed. The intention herein was to investigate performance differences between the organic (OLED, OPD) and inorganic (LED, PD) light sources and detectors.
Finally, measurements of heart- and respiration rate were executed by applying the MEMS sensor stack on the skin with adhesive tape and recording the signal with an oscilloscope.

3.3.1. MEMS characteristic

In order to measure the frequency response of the MEMS vibration sensor, a mechanical actuation (deflection) needs to be applied at a wide range of frequencies. For that purpose, a linear piezoelectric shaker unit [36] driven by a sinusoidal voltage from a frequency generator (Agilent 33220A) was used. The frequency was swept to record the transfer function around the resonance frequency f_r. By changing the amplitude of the driving voltage, the deflection of the oscillating metal plate could be chosen.
A green inorganic LED (Osram LT-T673-N2S1-35) was used as light source for the vibration sensor. The light was detected by an inorganic PD (Vishay Semiconductors,

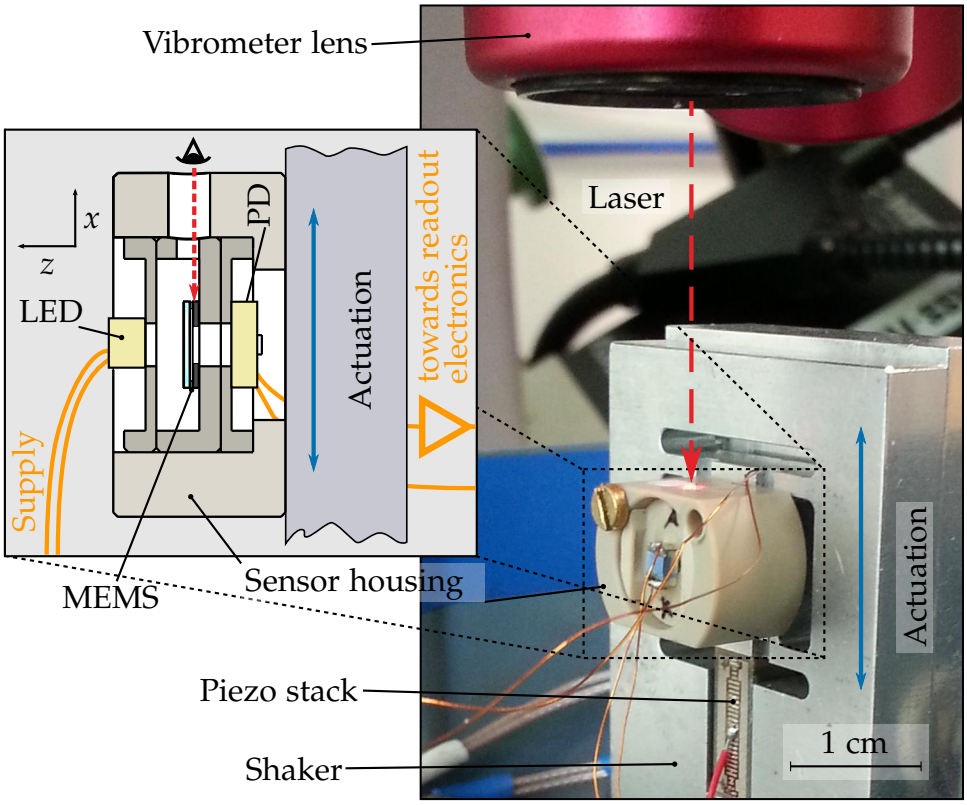

Figure 3.9.: Detailed view of the MEMS sensor housing mounted on the shaker unit. The laser beam enters the housing via an opening, which made it possible to measure the mechanical deflection directly at the MEMS frame [16].

TEMD5510FX01) after being modulated by the MEMS chip. The chip itself was mounted onto a plastic chip holder to ensure good alignment between LED and PD. These three components were stacked on top of each other (PD – MEMS chip – LED) in a custom-built housing and fixed to the shaker plate which provided a vertical actuation in this case. Thus, the MEMS sensor had to be oriented accordingly. A grounded metal cover shielded the shaker – MEMS sensor arrangement and the readout circuit from ambient light and electrical disturbances.

The input deflection of the MEMS frame was referenced by the LDV of a MSA-400 Micro System Analyzer from Polytec. This was enabled by a hole in the housing of the MEMS stack, which allowed the laser beam to reach the edge of the chip and detect the amplitude of the displacement directly at the place of interest. A lock-in amplifier (Stanford Research SR830) was used to record the analogue output signal of the vibrometer. Figure 3.9 gives an overview of the vibrometer measurement.

On the one hand, the reason for executing the LDV displacement measurements was

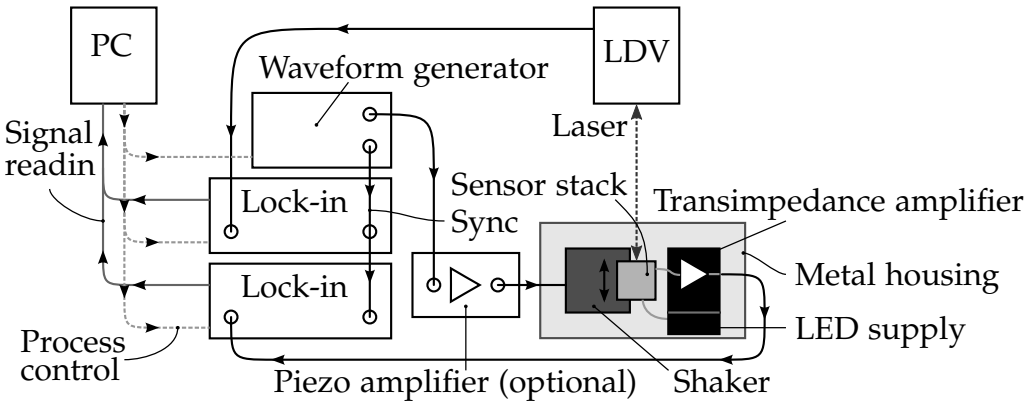

Figure 3.10.: Schematic of the sensor characteristic measurement setup using a laser-Doppler vibrometer (LDV) [16].

to correct possible eigenmodes of the shaker and/or sensor mounting, which may were excited. Therefore, prior to every measurement run a so called reference run had been performed, which was used during the measurement cycle to adjust the actuation voltage of the shaker. This minimised the effects of the eigenmodes [8]. On the other hand, the deflection was recorded in the measurement run to link the analogue output signal generated by the MEMS sensor with the input vibration, and hence, calculate the sensitivity S. This output voltage of the TIA circuit which originates from the modulated photocurrrent I_p was recorded by a second lock-in amplifier.
The measurement was controlled by a Python measurement script which governed the lock-ins and the frequency generator. Also the data storage was managed by the script. A detailed scheme of the complete measurement arrangement is shown in Fig. 3.10.

For measurements with the organic LEDs and PDs, the same setup could not be used, because the size of these elements is larger than the inorganic ones. Therefore, they could not be mounted in the same way and the LDV could not be used. Thus, only one lock-in amplifier was recording the modulated analogue output voltage of the TIA. The Python measurement script was slightly modified and the direction of actuation was changed to horizontal for a better mounting of the organic elements. The OPD as the bottom element was fixed by adhesive tape to a small plastic table which was mounted on the oscillating plate of the shaker. A two-component epoxy adhesive or adhesive tape was used to connect the MEMS chip with the glass surface of the OPD. A plastic plate with an opening for the sensor was also attached on the OPD. It served as the connection layer for the OLED which was fixed on top of it, again with adhesive tape. That way, a stack of OLED/ MEMS/ OPD was achieved analogous to the inorganic

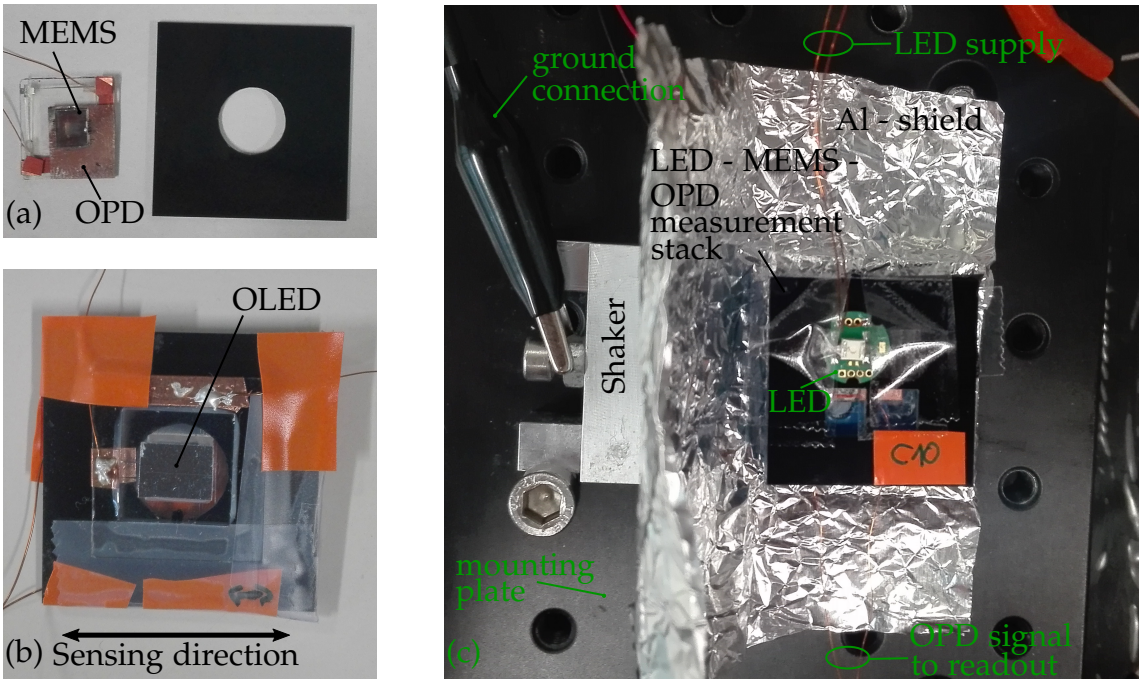

Figure 3.11.: (a) An OPD with a MEMS chip fixed above the sensitive area and the plastic plate with an opening in the centre to the right. (b) OPD – MEMS – OLED measurement stack held together by adhesive tape. (c) The measurement stack (comprising OPD – MEMS – LED) mounted onto the shaker plate by means of a plastic connection unit and adhesive tape. The Al shield is connected directly to the shaker and eliminates capacitive disturbances originating from the actuation voltage on the photocurrent produced by the OPD.

stack. An overview of the measurement setup using organic components is given in Fig. 3.11.

3.3.2. Analysis of readout circuit noise

In order to analyse the noise performance of the detection circuit, Fast Fourier Transformation (FFT) measurements of the detection circuit output signal were performed with a SR780 Network Analyser from Stanford Research Systems. The main focus of this subsection is to show the difference in noise performance between the modified detection circuit (1 MΩ feedback resistor and low-pass filter with $f_c = 10.6$ kHz) and the previously used detection circuit (10 kΩ feedback resistor and low-pass filter with $f_c = 106.1$ kHz). Therefore, measurements with both circuits were carried out. If not stated otherwise the measurements were done with following settings on the Network Analyser:

- 800 FFT Lines
- Root mean squared (RMS) averaging (tenfold)
- BMH windowing
- Power Spectral Density (PSD) units

Using PSD units means that the measured amplitudes in each frequency bin are normalised by the square root of the linewidth. The PSD is given in units of $\mathrm{dBV_{pk}}/\sqrt{\mathrm{Hz}}$ and the measured quantity is, therefore, the square root of the noise voltage spectral density $V_{\mathrm{NS}} = \sqrt{S(V)}$ and corresponds to noise voltage per square root Hertz.
The sensor package consists of the standard green inorganic LED as light source, the inorganic PD as photosensitive detection unit and a MEMS chip as active vibrating structure in between. An LED current of 4 mA is set and the sensor package is mounted on the shaker unit which is used in horizontal direction. The whole setup is shielded from surrounding light and electromagnetic disturbances by a grounded metallic box and also the detection circuit is placed in another metallic case. Aluminium foil was used to shield the measurement leads between the detection circuit and the sensor package to prevent interference with external disturbances. The output of the readout circuit was connected with the SR780 Network Analyser input by a coaxial cable.

3.3.3. Heart- and respiration rate

Measurements of heart- and respiration rate were carried out by simply applying the stack of (O)PD, MEMS and (O)LED on the skin of a test person (in this case myself) sitting in an upright position. Figure 3.12b shows the measurement stack incorporating an OPD, a MEMS chip and the standard green LED applied to the test person. Several measurement points on the wrist and the neck were tested, but the best one turned out to be on the neck, directly above the carotid artery. Both sensor stacks (organic and inorganic) were used and attached on the skin by adhesive tape. In the case of the OPD being used as the light detection module, the plastic sensor housing from the inorganic measurement setup in Subsec. 3.3.1 served as connection unit between skin and measurement stack (see Fig. 3.12a). This approach allowed a better fixation of the sensor stack to the body and induced a larger deflection of the MEMS sensor, which led to a better signal quality. The optical path of this setup lay in the sagittal axis, consequently the sensing direction was in the frontal plane in transversal orientation. In the case of using the inorganic LED and PD for the measurements, the sensor

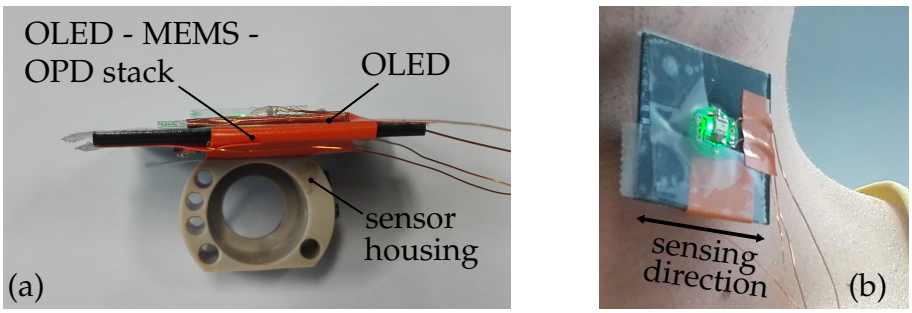

Figure 3.12.: (a) The measurement stack comprising organic elements which is mounted on top of the custom-built sensor housing, whereby a better displacement of the sensor's moving mass could be reached. (b) The sensor in action applied to the test person and measuring the heart - and respiration rate on the neck through actuation by the carotid artery.

housing comprising the measurement stack was directly fixed to the skin without any connection module. The optical path of the sensor stack was in vertical (longitudinal) direction and the sensing direction of the MEMS sensor lay sagittal (in the transversal plane). Various measurements with different orientations of sensor deflection had to be performed to find these optimal sensor operation directions.
LED and PD were connected to the readout circuit by the means of long shielded cables and the output signal of the TIA was observed and recorded by an oscilloscope (Tektronix TDS 2014B). Thereafter, the heart rate and respiration signals were analysed and plotted.

4. Results

4.1. Performance of the readout electronics

In this section, it is shown how the existing readout electronics was improved in terms of SNR. This way the signal quality of heart- and respiration rate (HR, RR) measurements was enhanced. For same MEMS sensors, this improvement enabled a successful measurement of HR and RR in the first place.
MEMS characteristic measurements were carried out with two MEMS chips (named J4 and C10) using the LDV setup from Subsec. 3.3.1 for measuring the transfer function of the transducers. Each measurement was performed two times, one time for the old (TIA amplification factor $A = 10^4$ V/A) and one time for the new readout circuit (TIA amplification factor $A = 10^6$ V/A). Figure 4.1 shows the respective transfer functions $S = V_{\text{out}}(\omega)/X_0$ (X_0 being the displacement amplitude measured by the LDV, which raises with increasing shaker excitation voltage V_{exc}) of the chip C10.
Each measurement consisted of three cycles, of which each one was conducted with a different actuation voltage of the shaker $V_{\text{exc}} = \{1, 2, 3\}$ V. An excitation voltage of $V_{\text{exc}} = 1$ V generates a deflection of the MEMS chip frame of $X_0 = 8.6$ nm, which was observed by the LDV measurements.
At frequencies outside of the noise region, the magnitude curves are overlapping for all actuation voltages and are seemingly merging into one curve. That can be explained by the linear dependency of the generated output voltage of the TIA on the input deflection, which leads to equal sensitivities S at different X_0 (see Subsec. 3.2.3). Thus, a higher output voltage V_{out} at $V_{\text{exc}} = 3$ V is divided by the higher amplitude of X_0, which leads to the same level of sensitivity S as for example in the case of $V_{\text{exc}} = 1$ V. Otherwise, the magnitude of S is dominated by the noise voltage of the electronics in the region of noise. This noise voltage is always on the same level, independent of the actuation voltage. Subsequently, calculating S leads to a lower level of sensitivity with higher input deflection, which explains why the curves do not overlap in the region of

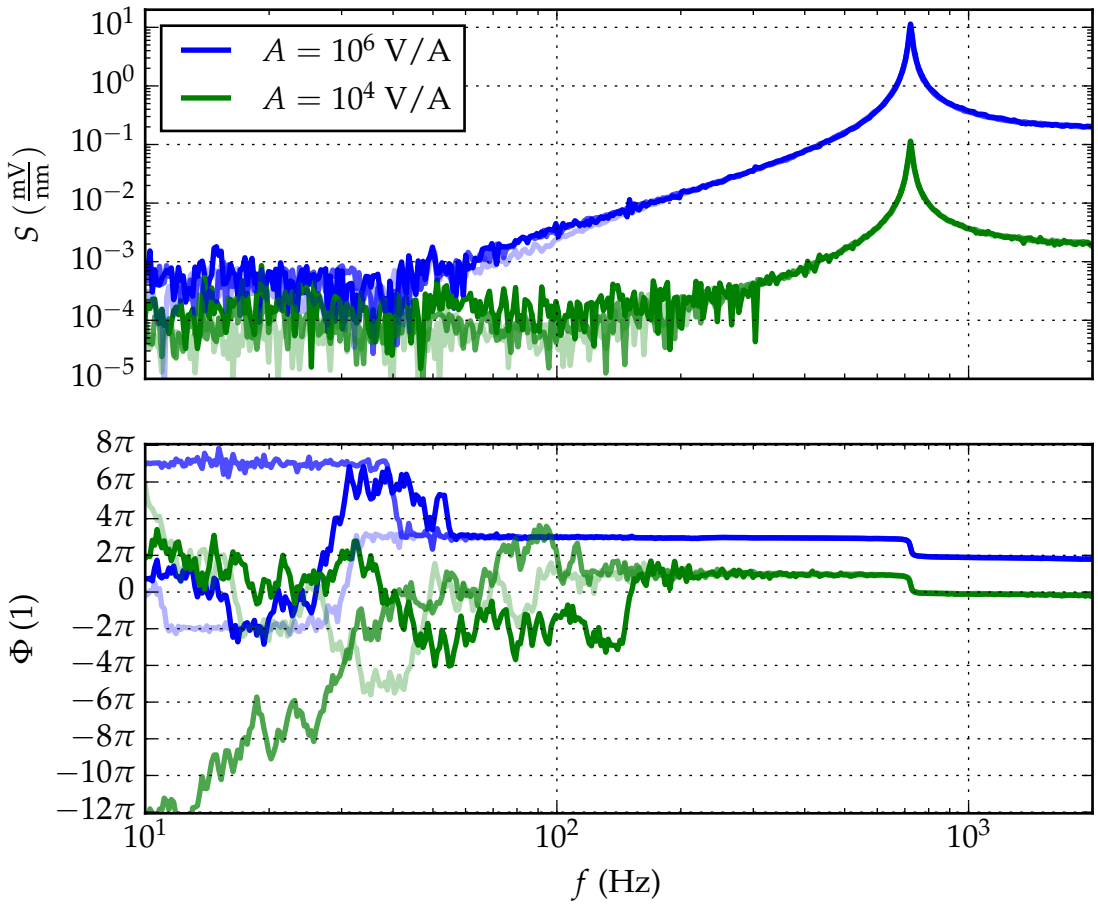

Figure 4.1.: Sensitivity (top) and phase information (bottom) of the new readout circuit (blue curves) compared to the old electronics (green curves) for the MEMS chip C10. The different cycles are plotted with lines of different transparency (the 3 V curve has the highest transparency value).

noise.

As can be seen from the plot, the measurement of the chip C10 shows the typical characteristic of the lumped parameter model with a high value of Q described in section 3.2.2). The typical phase jump by π in the phase plot is clearly visible at the resonance frequency $f_\mathrm{r} = 722$ Hz. It can be seen that the phase responses for the new and the old detection circuit are identical in the region outside of noise. Only for reasons of better visibility, they were shifted in vertical direction to each other. In the noisy region the unwrap algorithm of the python script generates the high phase values.

Looking at the noise level of the magnitude curves in the low frequency region, it

can be observed that the noise level of the new detection circuit is by a factor of approximately 10 higher compared to the old detection electronics. However, the actual signal ($f > 100$ Hz) has increased by a factor of 100. This is due to the enlarged feedback resistor R_f (1 MΩ instead of 10 kΩ) of the TIA in the readout electronics ($V_\mathrm{out} = I_\mathrm{p} R_\mathrm{f}$). The noise voltage has increased only by $\sqrt{{R_\mathrm{f}}^{new} / {R_\mathrm{f}}^{old}}$ according to the proportion of thermal noise (see Subsec. 2.4.4). Consequently, the SNR was improved by $\frac{{R_\mathrm{f}}^{new} / {R_\mathrm{f}}^{old}}{\sqrt{{R_\mathrm{f}}^{new} / {R_\mathrm{f}}^{old}}} = \sqrt{{R_\mathrm{f}}^{new} / {R_\mathrm{f}}^{old}} = 10 \equiv 20$ dB. Therefore, by choosing a higher value of R_f, the actual measurement range of the sensor can be extended, because lower frequencies become accessible for the same actuation amplitude.

4.2. Results of noise measurements

In Fig. 4.2 the results for FFTs (measured with the SR780 Network Analyser described in Sec. 3.3.2) up to 12.5 Hz and 800 Hz are plotted for the J4 MEMS chip ($f_\mathrm{r} = 623$ Hz). Both plots compare the data of the new detection circuit with the old one. The FFT up to 12.5 Hz (Fig. 4.2a) shows that the noise level of the adapted circuit lies slightly higher than that of the original circuit. It is also obvious that when approaching smaller frequencies, the difference between the two signals gets smaller and smaller. This is important, if heart rate or respiration signals are measured, because these signals have frequency ranges of about 1 Hz. The noise of a 1 Hz respiration signal would have approximately the same amplitude, regardless of which circuit is used for the measurement.

Clear differences between the new and the old detection circuit are depicted in Fig. 4.2b, which shows the data for a FFT up to 800 Hz. This measurement was performed with a shaker excitation frequency $f_\mathrm{exc} = 300$ Hz, an amplitude of the excitation voltage of $V_\mathrm{exc} = 1$ V and an offset voltage of $V_\mathrm{Off} = 0.5$ V. At the excitation, the amplitude of the new detection circuit has a value of $V_\mathrm{NS} = -60\ \mathrm{dBV_{pk}}/\sqrt{\mathrm{Hz}}$, whereas the one of the old detection circuit lies at $V_\mathrm{NS} = -100\ \mathrm{dBV_{pk}}/\sqrt{\mathrm{Hz}}$. The difference of $40\ \mathrm{dBV_{pk}}/\sqrt{\mathrm{Hz}}$ corresponds to the difference in the feedback resistors of the two circuits (1 MΩ compared to 10 kΩ).

The FFTs of both signals also show peaks at the second harmonic of the excitation frequency $f = 600$ Hz. These peaks differ in their amplitude also by approximately $40\ \mathrm{dBV_{pk}}/\sqrt{\mathrm{Hz}}$. In an area around the resonance frequency of the MEMS structure

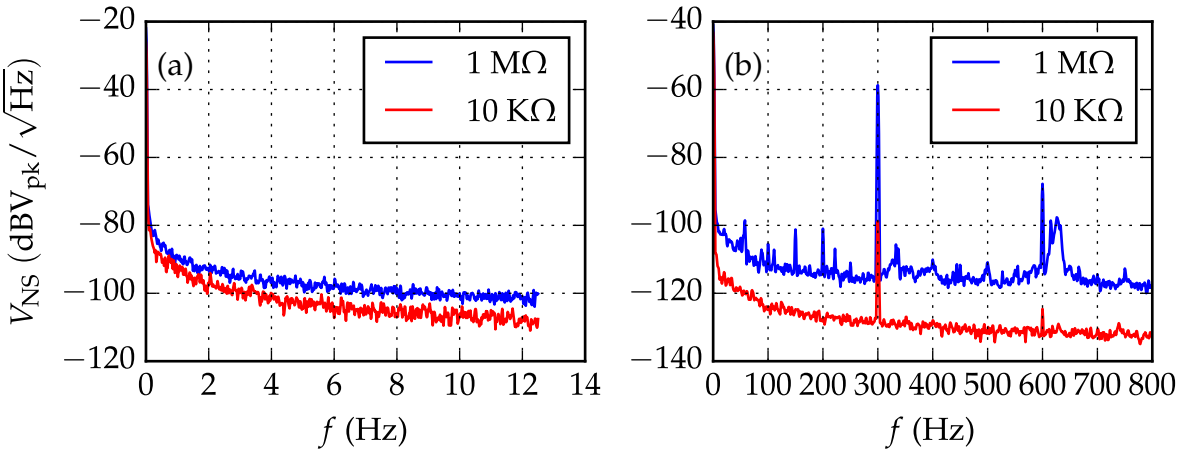

Figure 4.2.: (a) FFT until 12.5 Hz, (b) FFT until 800 Hz with shaker excitation at 300 Hz

(f_r = 623 Hz), another peak in the signal of the new detection circuit is present. This peak is not visible in the signal of the old detection circuit, which implies that the detection sensitivity of the new circuit is much higher compared to the old one. The level of the noise floor of the two signals at $f = 500$ Hz differs by approximately 20 dBV$_{pk}/\sqrt{Hz}$. This deviation can be explained by the different thermal noise voltages of the feedback resistors in the amplification circuits. The thermal noise voltage v_{tn} is given by Eq. (2.1). Since the feedback resistor of the new detection circuit is higher by a factor of 100 compared to the feedback resistor in the old detection circuit, the thermal noise voltage increases by a factor of $\sqrt{100} = 10 = 20$ dB.

In Fiq. 4.3, the FFTs of the new and the old detection circuit are plotted up to 102.4 kHz (in logarithmic scaling), which is the maximum measurement range of the network analyser. Data from six different measurements are put together to form one measurement curve for either noise signal. Each of the different measurement sequences is plotted in an individual colour. This approach was chosen to get a better resolution of the FFT measurements, because a measurement is limited to a maximum of 800 FFT points by the network analyser. No shaker excitement was used during these measurements.

The lower curve shows the noise level of the old detection circuit, whereas the upper one reveals the noise level of the new detection circuit. The difference between the noise levels is increasing with increasing frequency. From 0.1 Hz to 10 kHz (old detection circuit) and from 0.1 Hz to 1 kHz (new detection circuit), the measurement curves show a $1/f^{\alpha}$ behaviour, which means that $1/f^{\alpha}$ noise is dominating in these frequency

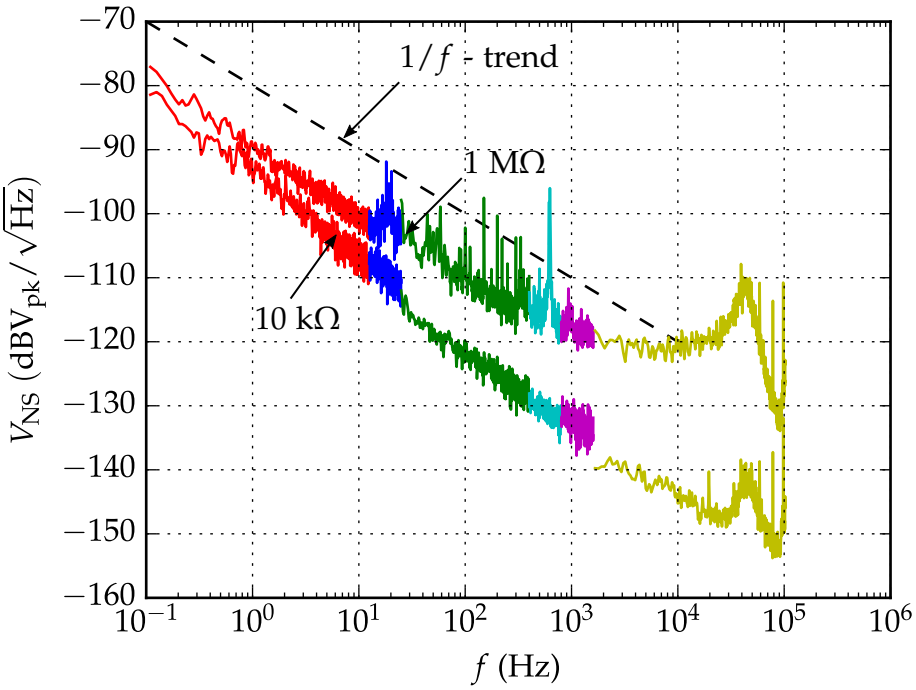

Figure 4.3.: FFTs of the new (upper curve) and old (lower curve) detection circuit up to 102.4 kHz compared to a $1/f$ trend

ranges. This behaviour can be explained by the $1/f^{\alpha}$ noise in low frequency regions of the LED and photodiode used in the sensor package. Many types of LEDs and photodiodes show typical $1/f^{\alpha}$ noise [37, 38] and therefore it is not surprising that the data in Fig. 4.3 represents this behaviour, too. In LEDs, as in the most semiconductor devices, these typical $1/f^{\alpha}$-type fluctuations originate from a superposition of many capture and release processes in the capture centres of the charge carriers with widely distributed relaxation times. These centres can be formed during the fabrication process of the devices or due to degradation by various defects in the device structure.
Obviously, the data of the new detection circuit shows some interferences with external noise sources. Noise voltage peaks are present around 20 Hz, 50 Hz and harmonics thereof (100 Hz, 150 Hz,...). All these peaks and fluctuations can not be seen in the data of the old detection circuit, although the measurements were carried out under identical outer circumstances (concerning shielding, protection from surrounding light, external noise sources). Therefore, it is supposed that the increased feedback resistance also leads to a higher amplification of external noise intensity (compared to the old detection circuit). Additionally, a peak at the resonance frequency of the MEMS structure

is visible, which again can be explained by the increased sensitivity of the readout. Another phenomenon, which can be observed in both measurement curves, is the noise peaking at frequencies of about 40 kHz to 50 kHz. This behaviour is caused by the internal parasitic capacitance and resistance of the photodiode in combination with the TIA, which leads to this special frequency dependent characteristic of the overall noise [31].
Figure 4.4 illustrates noise measurements of the old detection circuit and the new detection circuit up to 102.4 kHz on a linearly scaled x-axis. A third measurement shows the noise of the new detection circuit without the low-pass filter at the output (green measurement curve). It can be seen again that the noise amplitude of the old detection circuit is smaller by 20 $\mathrm{dBV_{pk}}/\sqrt{\mathrm{Hz}}$ or even more over the whole measurement range compared to the new detection circuit. The noise peaking characteristic, which was described above, is also clearly observable in all three measurement curves. A missing RC low-pass at the output of the TIA has an effect as shown with the green line in the plot. At about 10 kHz, the noise signal starts to rise steeper than the circuit which contains the RC low-pass (cutoff frequency $f_c = 10.6$ kHz). For higher frequencies, the difference between the two curves increases more and more, which means that high-frequency noise is damped less in the circuit without the low-pass.
In this plot, peaks in the noise voltage are present close to 20 kHz, 40 kHz, 60 kHz, 80 kHz, and 100 kHz in all three curves. Finding them in Fig. 4.3 with the logarithmic x-axis is not as easy as in Fig. 4.4, but they are existent there, too. The origin of these peaks is not clear up to know. It seems that they are a consequence of external disturbances, as they are also present if a FFT measurement with a plain coaxial cable (without detection circuit) connected to the input of the Network Analyzer is carried out.

4.3. Comparing inorganic to organic sensor setup

In this section, the difference in sensitivity of the MEMS vibration sensor comprising inorganic LED and PD compared to the setup using organic elements (OLED and OPD) is investigated. The measurements were conducted with the organic measurement setup described in Subsec. 3.3.1. In this case, the sensitivity S is calculated in terms of the output voltage divided by the excitation voltage of the shaker ($V_{\mathrm{out}}/V_{\mathrm{exc}}$), because no reference measurement value is available. During prior measurements with the

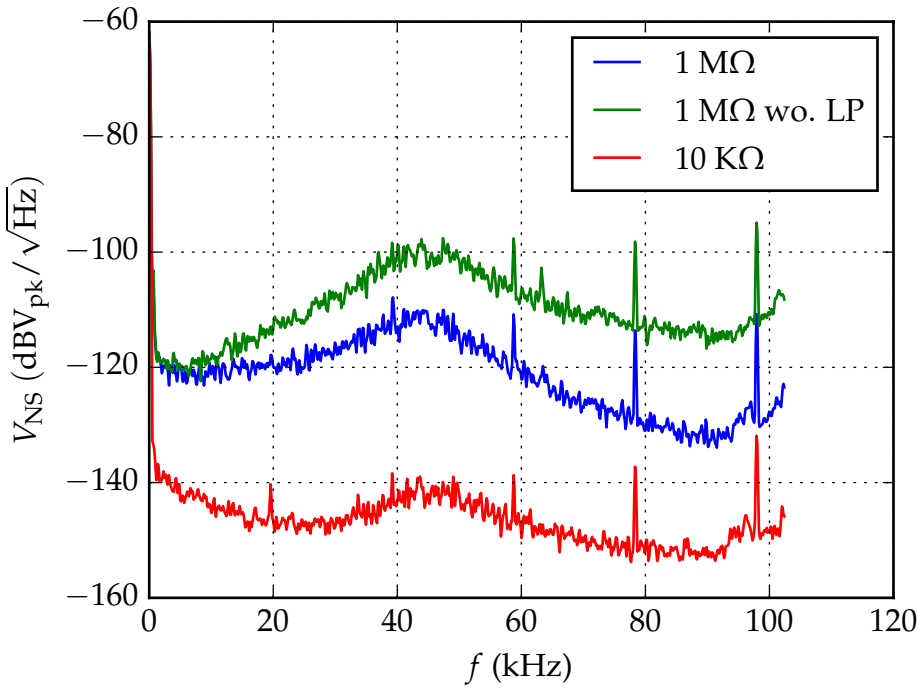

Figure 4.4.: FFT's of the output voltage V_{out} of different readout electronics configurations up to 102.4 kHz with linear scaling on the x-axis

LDV it was shown that 1V of actuation voltage led very reproducibly to an average deflection of 8.6 nm. Thus, the sensitivity derived from the input deflection in terms of $V_{out}(\omega)/X_0$ can be evaluated. This allows to compare sensitivity data from measurements with the LDV to data without the LDV in operation.

For each sensor setup (LED/PD, LED/OPD, OLED/OPD), measurements with differing actuation voltages of the shaker were executed. The results for the C10 MEMS chip are plotted in Fig. 4.5. All measurements were conducted with the same LED current ($I_{LED} = 4$ mA) driving the (O)LED and the improved readout electronics ($R_f = 1$ MΩ) was used. The first setup (red lines in the plot) used the standard green inorganic LED and the PIN photodiode. The data shows a similar behaviour as the data obtained with the LDV in Fig. 4.1, with a few exceptions. First of all, the peak sensitivity ($S_p = 20.65$ mV/nm at $V_{exc} = 1$ V) at the resonance frequency ($f_r = 722$ Hz) and therefore the whole sensitivity level is slightly higher compared to the sensitivity of C10 measured with the LDV ($S_p = 11.38$ mV/nm at $V_{exc} = 1$ V). The reason for this deviation is the changed measurement and sensor setup.

Secondly, disturbances of the sensitivity data are present at frequencies of 50 Hz and

150 Hz. These distortions stem from the DC power supply unit (Agilent E3631A), which provides the supply voltage for the readout electronics in this setup. A different power supply unit (Rohde & Schwarz HAMEG HMP2030), which did not generate these distortion signals, was used for the LDV measurements and, thus, they did not show up in the LDV measurement data.

For the vibration sensor comprising the standard green LED and an organic PD (green curves in Fig. 4.5), the sensitivity S is reduced. At the actuation voltage of $V_{\mathrm{exc}} = 0.5$ V the peak sensitivity drops to $S_{\mathrm{p}} = 5.35$ mV/nm by 75 % compared to the total inorganic setup. At $V_{\mathrm{exc}} = 1$ V the loss accounts for 77 % ($S_{\mathrm{p}} = 4.77$ mV/nm). These losses in sensitivity and thus sensor performance can be explained by several reasons. One cause of the decreased sensitivity is the chromium grid which is deposited on top of the glass cover of the OPD, which was intended to further miniaturise the sensor. By depositing the Cr grid directly onto the OPD, the glass chip of the MEMS can be omitted. First tests were executed to investigate the feasibility of that approach in Sec. 4.5.

For comparing organic to inorganic components, this additional grid on the OPD was obstructive and thus scratched off with the blade of a scalpel. As the grid could not be removed completely and scratches in the glass were formed, less light reached the sensitive area of the OPD, which lead to a lower sensitivity. Another problem is any misalignment in the light path between LED, MEMS chip and OPD. It was tough to align the MEMS chip oscillating mass (2×2 mm^2) by hand with the sensitive area of the OPD (3×3 mm^2) and the light emitting area of the LED. This fact lead to a lowered amount of light arriving at the OPD and therefore decreased sensitivity. At last, also a low quantum efficiency η_{q} of the OPDs material could be a reason for a lower sensitivity of the LED/ MEMS/ OPD stack.

The completely organic setup (blue curves in Fig. 4.5) exhibits the lowest sensitivity. At $V_{\mathrm{exc}} = 0.5$ V, the sensitivity is decreased by 82 % to $S_{\mathrm{p}} = 3.91$ mV/nm and at $V_{\mathrm{exc}} = 1$ V by 80 % to $S_{\mathrm{p}} = 4.23$ mV/nm compared to using inorganic elements. The effect of changing from an inorganic to an organic LED is recognised when the sensitivities of the blue curves are compared to the green ones. It is lower by 27 % at $V_{\mathrm{exc}} = 0.5$ V and 11 % at $V_{\mathrm{exc}} = 1$ V. This difference can be caused by an inaccurate placing of the OLED on the OPD/MEMS stack and the optical power of the OLED which is varying compared to the inorganic case. The exact technical parameters of the OLEDs/OPDs used are not known, because the manufacturer (NCTU, Taiwan) did

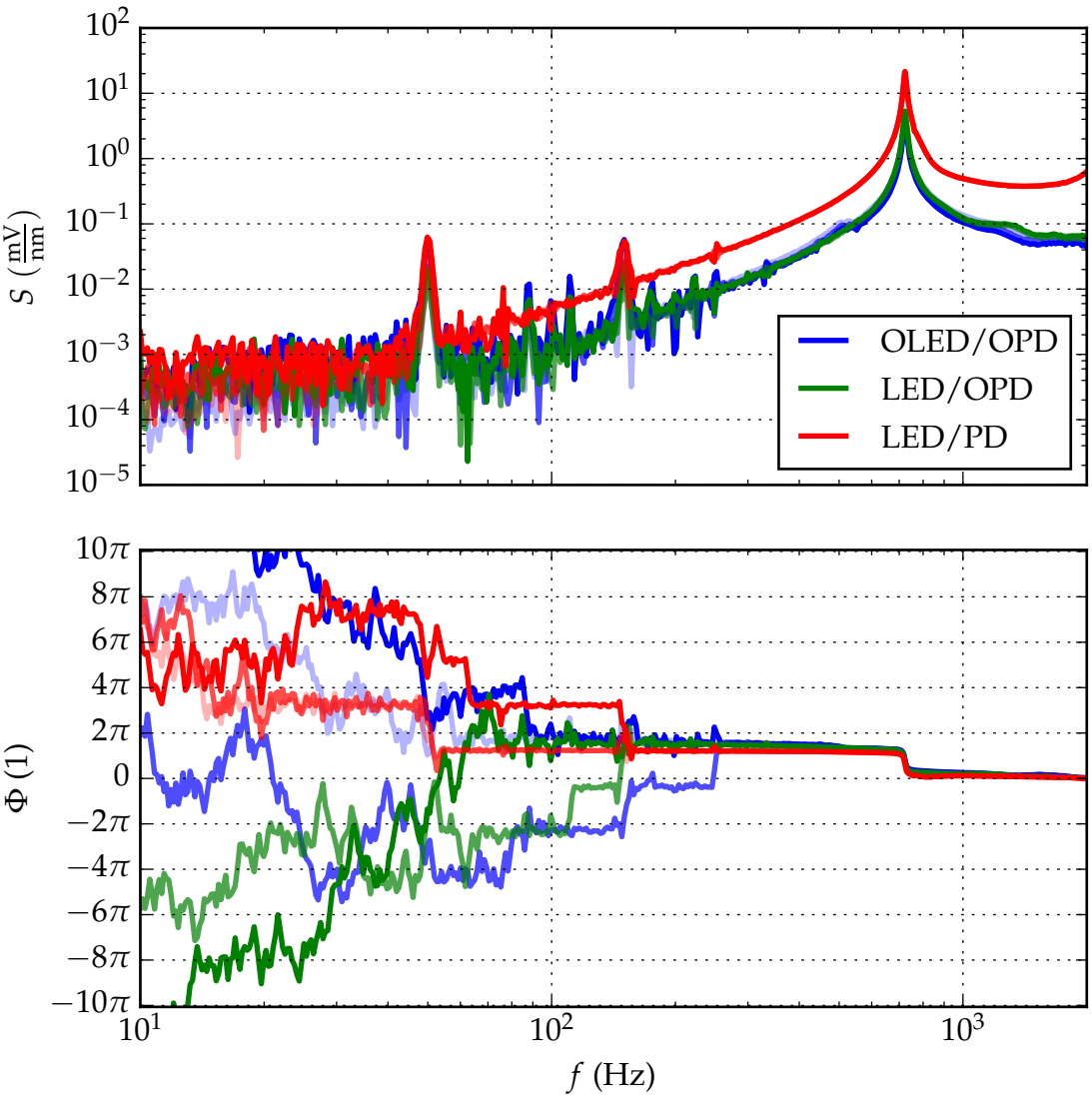

Figure 4.5.: Transfer characteristics with magnitude (top) and phase (bottom) of the MEMS chip C10. Different combinations of organic and inorganic light emitting and detection elements were used to investigate the difference in their performance. Measurements of one setup type are plotted in the same colour, but with different values of transparency. The measurements of the complete inorganic setup (red measurement curves) and the complete organic setup (blue measurement curves) were conducted with $V_{\mathrm{exc}} = \{0.5, 1, 2\}$ V, with the measurement curve of the highest transparency resulting from the highest actuation amplitude. The same is true for the setup using the inorganic LED and the OPD with $V_{\mathrm{exc}} = \{0.5, 1\}$ V.

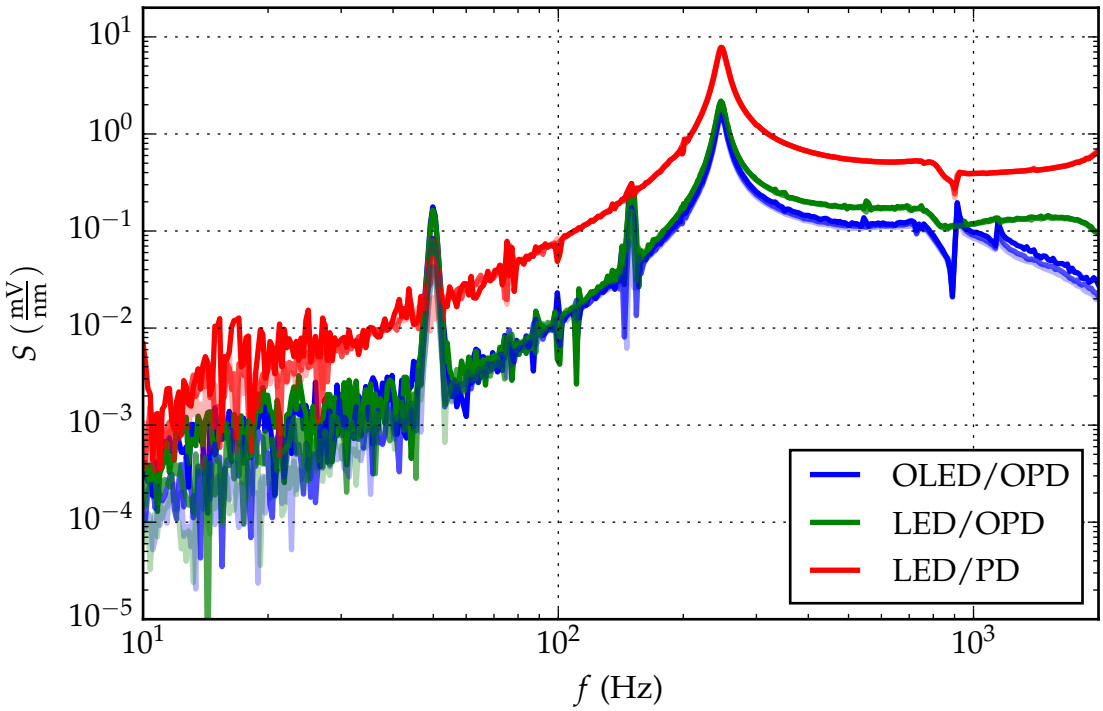

Figure 4.6.: Magnitude of the transfer characteristics of the MEMS chip H1. The curves in different colours correspond to different combinations of organic and inorganic light emission and detection elements. The measurements of all sensor setups were executed with $V_{\text{exc}} = \{0.5, 1, 2\}$ V. Each run is plotted in the colour of the associated setup, but with different line transparency (the most transparent line corresponds to 2 V actuation voltage).

not provide any related details of the organic components.

There is a relatively high variation in the sensitivity between the actuation voltages of $V_{\text{exc}} = 0.5$ V and $V_{\text{exc}} = 1$ V, with a much lower sensitivity at the lower actuation voltage. As the run with actuation voltage of 1 V was executed first, an explanation for that is the lowering of OLED emittance with every measurement cycle, which is shown in detail in Sec. 4.4

In Fig. 4.6 the magnitude of the transfer characteristic of the MEMS chip H1 is plotted. Again, for each sensor setup (LED/PD, LED/OPD and OLED/OPD) three measurement runs were executed for different actuation voltages $V_{\text{exc}} = \{0.5, 1, 2\}$ V. This MEMS chip is of special interest, because its resonance frequency is quite low ($f_{\text{r}} = 246$ Hz) compared to the chip C10, which makes it beneficial for the measurement of heart- and respiration rate, as will be shown in Sec. 4.6. The magnitude of the transfer characteristic shows the typical behaviour of the lumped parameter model in Subsec. 3.2.2, with the inorganic setup exhibiting the highest sensitivity and the organic

setup the lowest. In the organic case, the sensitivity is reduced by approximately 80 % with respect to the inorganic setup, similar to the chip C10. A detailed overview of the sensitivity data of the MEMS chip H1 and all the other sensor setups investigated in this thesis is given in Appendix A. All MEMS chips showed in principal the same behaviour of the sensitivity for the three different sensor setups as the chips C10 and H1.
In analogy to C10, electromagnetic disturbances introduced by the DC voltage supply were observed at 50 Hz and 150 Hz. Starting with about 800 Hz the measurement curves show a curious characteristic. An explanation for that is assumed to be the fixing of the MEMS chip on the OPD by adhesive tape instead of two component adhesive. This fixation method seems to cause this special spike of the sensitivity curves.

4.4. OLED performance

As mentioned above, the emittance of the OLED decreases with time. Figure. 4.7 shows the transfer functions of six subsequent measurements with the MEMS structure C10 carried out using the completely organic setup. Every measurement cycle lasted for approximately 60 minutes. The first run (red curve) yields a peak sensitivity of $S_\mathrm{p} = 4.28$ mV/nm, whereas at the last run the peak sensitivity drops to $S_\mathrm{p} = 3.11$ mV/nm which is a difference of 27 % in roughly six hours of operation. From that data it was extrapolated, that the OLED would stop working within several hours or at least after a few days in use. And indeed during this work it was observed that OLEDs suddenly stopped working. The worsening of the sensitivity can be explained by the decay of the organic light emitting material. A reduction of the LED current (from $I_\mathrm{LED} = 4$ mA to approximately $I_\mathrm{LED} = 0.5$ mA) would increase the lifetime of the OLED up to several weeks (information of the manufacturer after consultation). However, the drawback of lowering the LED current is a reduction in sensor sensitivity.

4.5. Performance of OPDs with chromium grating

All OPDs which were used during this thesis come with a chromium grating on the glass surface. In previous measurements this grating had to be removed (see Sec. 4.3), because there was already one on the glass chip of the MEMS. In this section, it is

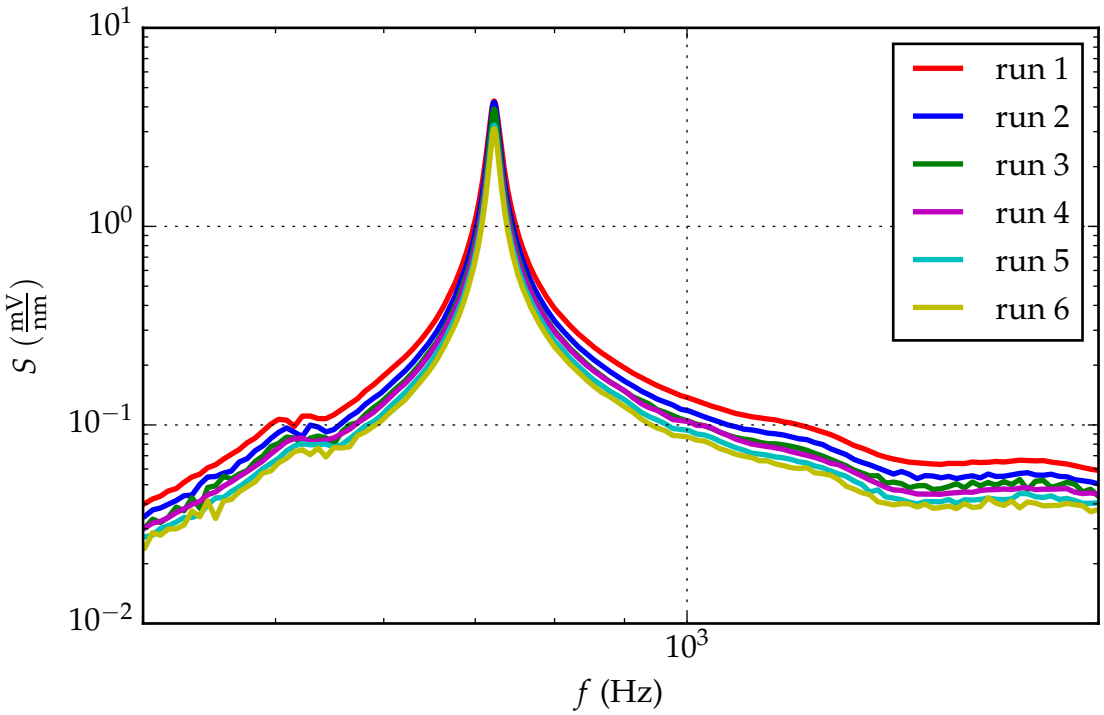

Figure 4.7.: Series of consecutive recorded transfer functions of the OLED/C10/OPD stack, showing a steady decrease of sensitivity with every measurement cycle owed to the decay of the OLED material.

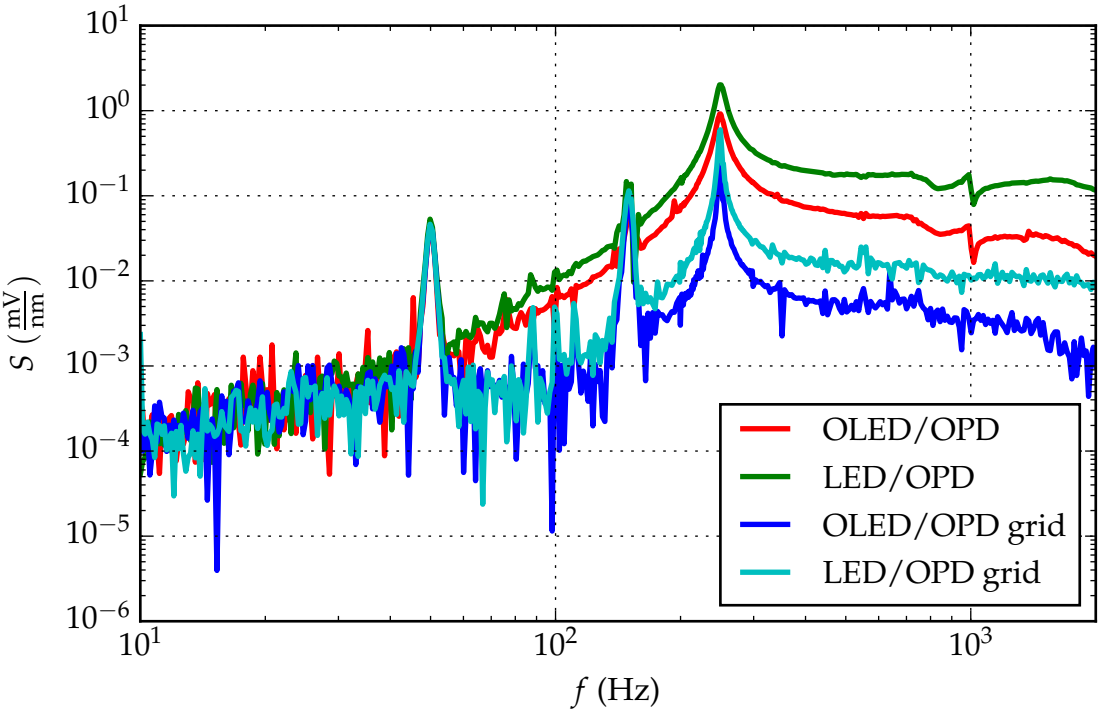

Figure 4.8.: Comparison of sensitivity data of MEMS chip F9 using an OPD with grid and a grid-less OPD. For each configuration at first the green standard LED and afterwards the OLED was used as light source . The shaker excitation voltage was set to $V_{\text{exc}} = 2$ V and the LED current to $I_{\text{LED}} = 4$ mA.

shown how this approach for further miniaturisation affects the sensor performance. In a first step, the glass chip which is bonded to the silicon chip had to be removed. This was done with a thin scalpel blade. It was critical to apply only small mechanical forces in order to avoid damage to the silicon chip. Afterwards, the silicon chip was fixed on the OPD glass surface with adhesive tape. The chromium grating of the OPD and the moveable mass were facing each other now, separated only by the tape. A MEMS chip with the same type of grating – hole dimension 20 µm×100 µm and distance $d_{\text{h}} = 20$ µm – was selected (F9). Another critical point was the correct alignment of the two gratings, which should be such that the holes overlap in a parallel way and by half of their area in the resting position. The alignment was done by hand with the help of a microscope. In Fig. 4.8, the outcome of this setup is depicted comparing the transfer functions using the OPD with grating to the transfer functions using the OPD without grating.

Two measurements were executed with the grid-less OPD, one time using the conven-

tional green LED and the other time the green organic LED. The same procedure was applied for the OPD incorporating the chromium grid. In both cases, the sensitivities of the measurement runs using the OLED are decreased compared to the measurements using the inorganic LED. This agrees with the findings in Sec. 4.3 depicted in Fig. 4.6. The comparison of OPD with grid and grid-less OPD revealed that the compact setup yielded a lower sensitivity. The low sensitivity is assumed to be caused by a poor alignment of the two gratings by hand. Even though strong effort was invested to achieve a good alignment, it was almost impossible to align the gratings parallel and without an offset in y-direction to each other. For a better result, different ways of alignment have to be found in the future.
External disturbances appear very strong in this data, because all the sensitivities are very low. The typical course of the vibration sensor transfer function can barely be recognised. However, the resonance peak is still clearly visible and the resonance frequency $f_\mathrm{r} = 249$ Hz can be identified.

4.6. Heart- and respiration rate measurement

At first it was tried to measure the heart rate by applying the inorganic sensor stack on the wrist. The MEMS chip H1 ($f_\mathrm{r} = 247$ Hz) was used in that approach and showed no good signal quality. It was not possible to obtain any information about the heart rate from that signal. The excitation of the sensor by the pulsating artery at the wrist was too weak to generate an appropriate signal. Therefore, it was decided to change the position of measurement to the neck. Double-sided adhesive tape was used to fix the sensor package above the carotid artery in a way that the optical path of the sensor lay in the vertical direction. This led to a excitation of the seismic mass of the MEMS in the direction of the sagittal axis (transversal actuation plane). The signal quality of the sensor was improved in this position, which enabled the detection of the heart- and respiration rate. But still the exact positioning of the sensor directly above the pulsating artery played a big role in terms of signal quality. Thus, in some attempts, it was not possible to obtain the respiration rate and in others, hardly any information could be gained.
A measurement in which the positioning yielded a good result is shown in Fig. 4.9. There, the output signal of the readout electronics V_sig is plotted (blue curve) for the MEMS chip H1 in inorganic configuration ($I_\mathrm{LED} = 4$ mA). The strongly pronounced

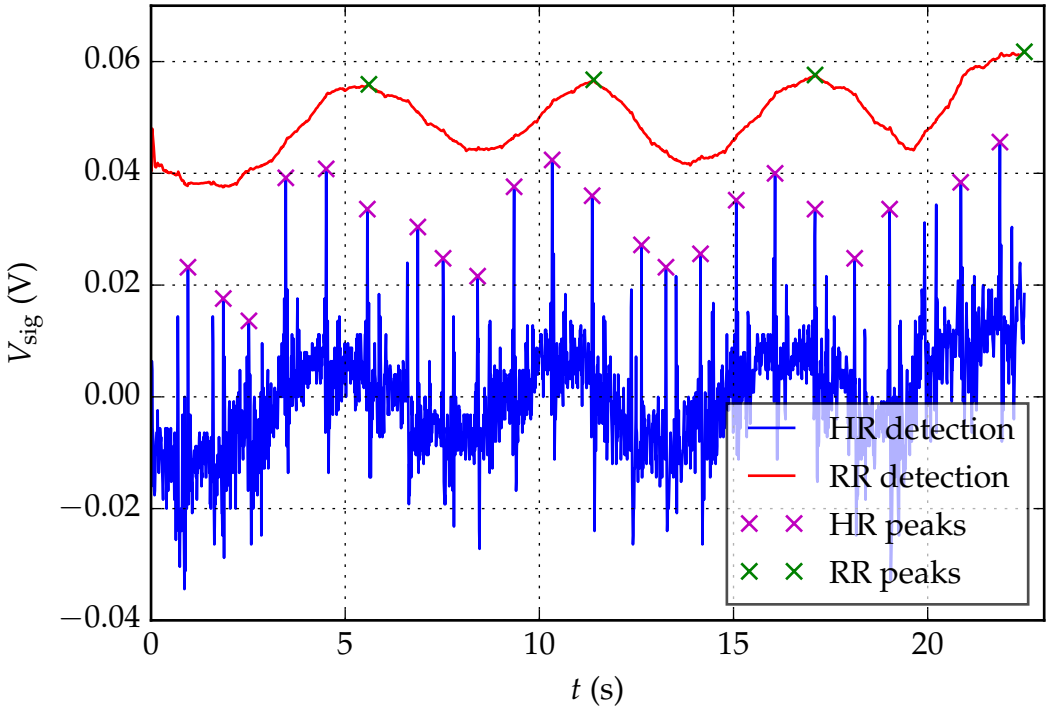

Figure 4.9.: Heart- and respiration rate signal obtained by the inorganic sensor setup using the H1 MEMS chip. The raw data (blue curve) is used for the detection of the heart rate. The red curve was obtained by applying a moving average filter and adding an arbitrary constant to the raw data. This signal shows the respiration. The magenta and green marks show the heart rate and respiration peaks resulting from the detection algorithm, respectively.

spikes in the raw signal each correspond to a pulsation of the carotid artery. A Python script was used to detect the individual peaks and calculate the mean heart rate out of the mean time difference between two adjacent peaks. The detection algorithm computed a mean heart rate of $HR_{\text{mean}} = 63.55$ beats/min with a standard deviation of $\sigma_{\text{HR}} = 14.37$ beats/min.

In addition to the heart rate, the raw data contains information about the respiration. The heart rate spikes are superimposed with the slower respiration rate, which is clearly visible in the blue curve. In order to find the respiration rate, a moving average filter was applied on the raw data, which smoothed the signal (red curve shifted by an arbitrary constant due to better visibility). From this curve, the mean respiration rate $RR_{\text{mean}} = 10.67$ respirations/min and the corresponding standard deviation $\sigma_{\text{RR}} = 0.33$ respirations/min were calculated.

Afterwards, measurements with MEMS chips having a higher resonance frequency (J4, $f_{\text{r}} = 622$ Hz and A6, $f_{\text{r}} = 618$ Hz) were executed. Both attempts yielded a signal in

which neither the respiration rate, nor the heart rate could be detected. The resonance frequency of these MEMSs is too high and therefore, the sensitivity of these chips is too low in the respective range of pulse- and respiration rate measurement ($f \lesssim 3$ Hz). Hence, for further measurements these MEMS chips were sorted out and only structures with low resonance frequencies like H1 and H3 ($f_\mathrm{r} = 258$ Hz) were used.
Another factor was the current driving the LED. A higher LED current increases the sensitivity of the sensor and improves signal quality. Measurements with $I_\mathrm{LED} = 4$ mA and $I_\mathrm{LED} = 20$ mA were executed and showed an increased signal at the higher current, but the difference was not breathtaking. Because of a faster ageing of the organic material of OLEDs with higher currents, it was decided to set the (O)LED current to 4 mA throughout further measurements.
At the same position (neck, above the left carotid artery), heart and respiration rate were measured with an organic sensor configuration, using OLED, MEMS and OPD. Due to the lower sensitivity of this setup (see Sec.4.3), that was challenging. Many attempts showed no information about pulse or respiration in the signal. Thus, it was necessary to increase the coupling of the heart- and respiration rate to the organic sensor stack, which was achieved by using the plastic sensor housing (from the inorganic setup) as a lever (see Fig. 3.12). This yielded a stronger actuation of the seismic mass. The raw and filtered data for the detection of the heart- and respiration rate by the H1 MEMS chip are plotted in Fig. 4.10 ($HR_\mathrm{mean} = 60.32$ beats/min and $\sigma_\mathrm{HR} = 14.07$ beats/min, $RR_\mathrm{mean} = 11.57$ respirations/min and $\sigma_\mathrm{RR} = 0.48$ respirations/min).
Compared to the raw signal of the inorganic setup, the amplitudes of the heart rate spikes are much smaller. Thus, a correct evaluation of the heart rate is difficult. This fact can have various reasons, beginning with the placement of the sensor package on the skin. The general lower sensitivity of the organic configuration, mentioned above, is another cause. Furthermore, the sensing direction of the sensor which is given by the orientation of the sensor on the skin. It lies in the frontal plane (transversal direction) and could lead to a weaker excitation of the oscillator. In the inorganic sensor setup the deflection direction of the pulse wave amplitude and the sensing direction of the vibration sensor are both in the transversal plane (sagittal direction), which probably has the consequence of an improved signal quality. Because of the larger dimensions of OLED and OPD it is difficult to apply the organic setup in the same way on the skin as the inorganic. But if a solution for this problem is found, it should be possible to increase the signal quality also for the organic measurement technique.

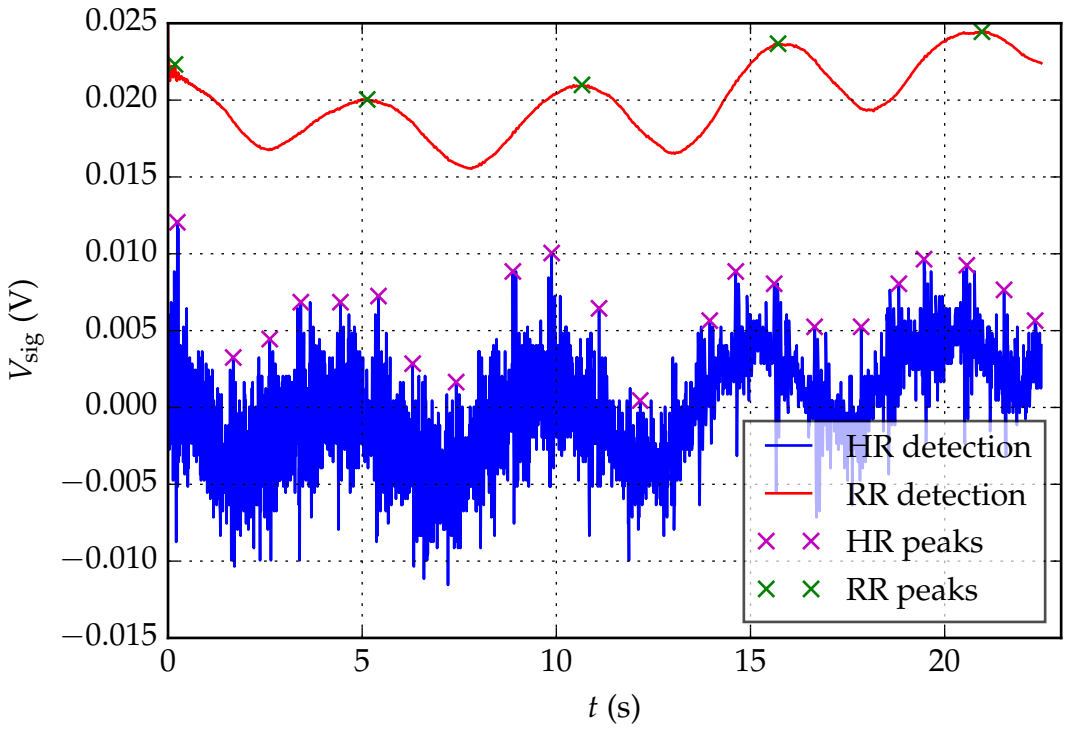

Figure 4.10.: Heart- and respiration rate signal obtained by the organic sensor setup using the H1 MEMS chip. The details of the plot are according to Fig. 4.9.

5. Discussion and outlook

In this thesis, a MEMS vibration sensor with optical readout was investigated for the measurement of pulse and respiration rate at humans. The electronic circuit for reading out the sensor was adapted to the detection via photodiodes. Therefore, the feedback resistance R_f of the TIA was increased from 10 KΩ to 1 MΩ. The accompanied theoretically predicted increase of the signal to noise ratio (SNR) by 20 dB was achieved, which is shown in the measurements in Sec. 4.1 and Sec. 4.2. But there is room for enhancing the performance of the electronic readout, because it is still limiting the resolution of the sensor. The theoretical limit of resolution is set by the Brownian noise of the sensor, given by the mean noise force $F_{th} = \sqrt{4k_B Td}$ [16]. With the actual readout electronics it is not possible to reach this resolution limit and thus, great effort should be invested in the future to develop a more sophisticated readout circuit.
The transfer from the inorganic sensor setup to the organic configuration worked, but there are still several issues which have to be solved. Using organic optoelectronics lead to a decreased sensor performance (shown in Sec. 4.3). The reasons for that decreased sensitivity are diverse, but for sure the alignment of OLED, MEMS chip and OPD plays an important role. A perfect arrangement is difficult to be achieved by hand and thus, only portions of the complete OLED emittance reach the OPD. Additionally, the removing of the grating on the OPD glass substrate leads to scratches on it. Therefore, it is not perfectly translucent and evokes sensitivity losses. A promising idea for the future is to get rid of the MEMS glass chip and use the Cr grid on the OPD (or even on the OLED) instead (see Sec. 4.5). For a perfect implementation, it is necessary to combine the fabrication of the MEMS chips and the organic semiconductors into one process. By doing so, the alignment problems between the grids and the light emitting/ sensitive areas could be solved by the higher precision of micromachining. Even the structuring of the emitting OLED area as a grid similar to the Cr grid (but in negative structure) seems possible [10]. It will reduce the active OLED area and thus, decrease power consumption. Omitting the stationary Cr mask would also be an advantage

of this approach. Further improvements of combining organic optoelectronics with MEMS chips are a higher compactness of the sensor and a more homogeneous light distribution of the light source. Organic optoelectronics have also advantages in the production of thin large-area devices and the patterning on flexible substrates, which could be interesting for wearable devices. Supplementary, they benefit from cheaper processing methods.

The lifetime of OLEDs is another issue. Measurements in Sec. 4.4 showed that the sensitivity of the vibration sensor setup with OLEDs decreases with every measurement cycle, which implies that the OLED emittance is fading. This can be explained by the decay of the light emitting material which is induced by oxidation and humidity. Further research and development is needed for a better encapsulation of OLEDs and OPDs to overcome this problem.

By attaching the MEMS sensor in inorganic configuration on the skin above the carotid artery on the neck, it was shown that heart- and also respiration rate can be measured via the pulsatile blood waves and respiration movements. Measurements in Sec. 4.6 showed that MEMS with a resonance frequency of about 620 Hz did not yield a good quality signal. The sensitivity of such structures in the frequency range of pulse and respiration is too low. Therefore, MEMS chips with lower resonance frequencies ($f_\mathrm{r} \sim 250$ Hz) were chosen. The signal quality was improved and heart- and respiration rate could be obtained. A drawback of the low resonance frequency (reached by higher mass m of the oscillator and lower spring constant k) is the decreased mechanical stability of the MEMS structure. This explains, why f_r can not be lowered arbitrarily.

When using organic components for the readout, the measurement was more difficult because of their lower sensitivity. The different orientation of the organic sensor on the skin (compared to the inorganic setup) may also be a reason for that, outlined in Sec. 4.6.

More challenges for an employment of the sensor in an actual application are the proper fixation on the skin, as well as the immunity to any other mechanical actuations, like vibrations from normal movement or gait. Here, the usage of two sensors and a differential evaluation of their signals would be an idea. Furthermore, for a comfortable application a wireless interface to a smart watch, smart phone or any other device analysing and displaying the health parameters would be necessary.

Appendix

A. MEMS chip sensitivity data

In this appendix, the different sensor setups LED – MEMS – PD, LED – MEMS – OPD and OLED – MEMS – OPD are compared to each other regarding their sensitivity. The following tables show the peak sensitivities S_p for each excitation voltage V_{exc} of the MEMS chips C10, J4, J0, H1, F9 and I10. By these values, the relative deviation in sensor sensitivity between the inorganic setup and the setup using the LED and the OPD is calculated by ΔS_{p1}. The relative deviation between the inorganic and the organic setup is given by ΔS_{p2}, whereas by ΔS_{p3} the relative deviation if exchanging the LED by an OLED is given. All MEMS chips show in principle the same behaviour, with the highest sensitivity in the inorganic case and the lowest with the organic setup. ΔS_{p3} shows additionally the decay of the OLED material, by an increasing deviation with advancing time (the measurement with the lowest excitation voltage was conducted first in a usual experiment). Also for the chips C10 (Tab. A.1) and J4 (Tab. A.2) ΔS_{p3} is increasing with advancing time, because the experiment for the organic setup was started with the highest excitation voltage.

Table A.1.: Sensitivity data and relative deviations in sensor sensitivity for different setups of the MEMS chip C10 with f_r =722 Hz.

C10	V_{exc} (V)	S_p (mV/nm)	ΔS_{p1} (%)	ΔS_{p2} (%)	ΔS_{p3} (%)
LED/PD	0.5	21.58			
	1	20.65			
LED/OPD	0.5	5.35	75.21		
	1	4.77	76.90		
OLED/OPD	0.5	3.91		81.88	26.92
	1	4.23		79.52	11.32

Table A.2.: Sensitivity data and relative deviations in sensor sensitivity for different setups of the MEMS chip J4 with f_r =623 Hz.

J4	V_{exc} (V)	S_p (mV/nm)	ΔS_{p1} (%)	ΔS_{p2} (%)	ΔS_{p3} (%)
LED/PD	0.5	21.05			
	1	21.12			
LED/OPD	0.5	11.06	47.45		
	1	11.27	46.63		
OLED/OPD	0.5	7.07		66.40	36.07
	1	8.01		62.07	28.93

Table A.3.: Sensitivity data and relative deviations in sensor sensitivity for different setups of the MEMS chip J0 with f_r =946 Hz.

J0	V_{exc} (V)	S (mV/nm)	ΔS_1 (%)	ΔS_2 (%)	ΔS_3 (%)
LED/PD	0.5	31.86			
	1	30.41			
	2	25.67			
LED/OPD	0.5	16.38	48.58		
	1	15.54	58.88		
	2	13.13	48.85		
OLED/OPD	0.5	8.12		74.50	50.42
	1	6.61		78.25	57.45
	2	4.80		81.30	63.44

Table A.4.: Sensitivity data and relative deviations in sensor sensitivity for different setups of the MEMS chip H1 with f_r =246 Hz.

H1	V_{exc} (V)	S (mV/nm)	ΔS_1 (%)	ΔS_2 (%)	ΔS_3 (%)
LED/PD	0.5	7.79			
	1	7.75			
	2	7.90			
LED/OPD	0.5	2.19	71.89		
	1	2.15	72.26		
	2	2.13	73.04		
OLED/OPD	0.5	1.66		78.69	24.20
	1	1.58		79.61	26.51
	2	1.49		81.14	30.05

Table A.5.: Sensitivity data and relative deviations in sensor sensitivity for different setups of the MEMS chip F9 with f_r =250 Hz.

F9	V_{exc} (V)	S (mV/nm)	ΔS_1 (%)	ΔS_2 (%)	ΔS_3 (%)
LED/PD	0.5	6.45			
	1	6.47			
	2	6.52			
LED/OPD	0.5	2.15	66.66		
	1	2.02	68.73		
	2	2.02	69.08		
OLED/OPD	0.5	1.13		82.47	47.42
	1	0.99		84.67	50.99
	2	0.92		85.91	54.44

Table A.6.: Sensitivity data and relative deviations in sensor sensitivity for different setups of the MEMS chip I10 with f_r =275 Hz.

I10	V_{exc} (V)	S (mV/nm)	ΔS_1 (%)	ΔS_2 (%)	ΔS_3 (%)
LED/PD	0.5	5.27			
	1	5.26			
	2	5.26			
LED/OPD	0.5	2.08	60.44		
	1	2.05	60.96		
	2	2.03	61.34		
OLED/OPD	0.5	1.44		72.64	30.85
	1	1.36		74.09	33.64
	2	1.30		75.34	36.20

Bibliography

[1] E. Blazer, W. Koh and E. Yon. 'A miniature digital pressure transducer'. In: *24th Annu. Conf. Engineering Medicine and Biology*. 1971, p. 211.

[2] Gregory T. Kovacs. *Micromachined Transducers Sourcebook*. McGraw-Hill Science/Engineering/Math, 1998. ISBN: 0-07-290722-3.

[3] David J. Monk. *MEMS physical sensors for automotive applications*.

[4] Shekhar Bhansali and Abhay Vasudev. *MEMS for biomedical applications*. Woodhead Publishing, 2012. ISBN: 978-0-85709-129-1.

[5] N. Barbour and G. Schmidt. 'Inertial sensor technology trends'. In: *IEEE Sensors Journal* 1.4 (2001), pp. 332–339. DOI: 10.1109/7361.983473.

[6] Babak Vakili Amini and Farrokh Ayazi. 'Micro-gravity capacitive silicon-on-insulator accelerometers'. In: *Journal of Micromechanics and Microengineering* 15.11 (Sept. 2005), pp. 2113–2120. DOI: 10.1088/0960-1317/15/11/017.

[7] N.A. Hall et al. 'Micromachined Accelerometers With Optical Interferometric Read-Out and Integrated Electrostatic Actuation'. In: *Journal of Microelectromechanical Systems* 17.1 (Feb. 2008), pp. 37–44. DOI: 10.1109/jmems.2007.910243.

[8] Wilfried Hortschitz et al. 'An Optical In-Plane MEMS Vibration Sensor'. In: *IEEE Sensors Journal* 11.11 (Nov. 2011), pp. 2805–2812. DOI: 10.1109/jsen.2011.2169781.

[9] Wilfried Hortschitz et al. 'Robust Precision Position Detection With an Optical MEMS Hybrid Device'. In: *IEEE Transactions on Industrial Electronics* 59.12 (Dec. 2012), pp. 4855–4862. DOI: 10.1109/tie.2011.2173096.

[10] Thilo Sauter et al. 'Making optical MEMS sensors more compact using organic light sources and detectors'. In: *Proceedings of the 2014 IEEE Emerging Technology and Factory Automation (ETFA)*. IEEE, Sept. 2014. DOI: 10.1109/etfa.2014.7005342.

[11] Eugenijus Kaniusas. *Biomedical Signals and Sensors I*. Springer Berlin Heidelberg, 2012. DOI: 10.1007/978-3-642-24843-6.

[12] Eugenijus Kaniusas. *Biomedical Signals and Sensors II: Linking Acoustic and Optic Biosignals and Biomedical Sensors (Biological and Medical Physics, Biomedical Engineering)*. Springer, 2015. ISBN: 978-3-662-45106-9.

[13] Marcin Kielar et al. 'Long-Term Stable Organic Photodetectors with Ultra Low Dark Currents for High Detectivity Applications'. In: *Scientific Reports* 6.1 (2016). DOI: 10.1038/srep39201.

[14] Ross D. Jansen-van Vuuren et al. 'Organic Photodiodes: The Future of Full Color Detection and Image Sensing'. In: *Advanced Materials* 28.24 (2016), pp. 4766–4802. DOI: 10.1002/adma.201505405.

[15] You Seung Rim et al. 'Recent Progress in Materials and Devices toward Printable and Flexible Sensors'. In: *Advanced Materials* 28.22 (2016), pp. 4415–4440. DOI: 10.1002/adma.201505118.

[16] Andreas Kainz. 'Optimisation of an Optomechanical Transducer and its Aplication as Electric field sensor'. PhD thesis. Institute of Sensor and Actuator systems, 2017.

[17] Ekbert Hering and Rolf Martin. *Photonik: Grundlagen, Technologie und Anwendung (German Edition)*. Springer, 2005. ISBN: 3-540-23438-1.

[18] Georg A. Reider. *Photonik: Eine Einführung in die Grundlagen (German Edition)*. Springer, 2013. ISBN: 978-3-7091-1520-6.

[19] K. Kudo and T. Moriizumi. 'Spectrum-controllable color sensors using organic dyes'. In: *Applied Physics Letters* 39.8 (1981), pp. 609–611. DOI: 10.1063/1.92820.

[20] Gordon J. Hedley et al. 'Determining the optimum morphology in high-performance polymer-fullerene organic photovoltaic cells'. In: *Nature Communications* 4 (2013). DOI: 10.1038/ncomms3867.

[21] Sung Heum Park et al. 'Bulk heterojunction solar cells with internal quantum efficiency approaching 100%'. In: *Nature Photonics* 3.5 (2009), pp. 297–302. DOI: 10.1038/nphoton.2009.69.

[22] G. Yu et al. 'Polymer Photovoltaic Cells: Enhanced Efficiencies via a Network of Internal Donor-Acceptor Heterojunctions'. In: *Science* 270.5243 (1995), pp. 1789–1791. DOI: 10.1126/science.270.5243.1789.

[23] Gabriel Vasilescu. *Electronic Noise and Interfering Signals. Principles and Applications*. Berlin Heidelberg: Springer-Verlag, 2005. DOI: 10.1007/b137720.

[24] W. Schottky. 'Über spontane Stromschwankungen in verschiedenen Elektrizitätsleitern'. In: *Annalen der Physik* 362.23 (1918), pp. 541–567. DOI: 10.1002/andp.19183622304.

[25] Aldert Van der Ziel. *Noise: Sources, Characterization, Measurements*. New Jersey: Prentice-Hall, 1970.

[26] F.N. Hooge. '1/f noise'. In: *Physica B+C* 83.1 (1976), pp. 14–23. DOI: 10.1016/0378-4363(76)90089-9.

[27] F.N. Hooge. '1/f noise sources'. In: *IEEE Transactions on Electron Devices* 41.11 (1994), pp. 1926–1935. DOI: 10.1109/16.333808.

[28] Leendert Bliek. 'A model for 1/f noise'. In: *IEEE Transactions on Instrumentation and Measurement* IM-30.4 (1981), pp. 307–309. DOI: 10.1109/tim.1981.6312419.

[29] L. Forbes. 'On the theory of 1/f noise of semi-insulating materials'. In: *IEEE Transactions on Electron Devices* 42.10 (1995), pp. 1866–1868. DOI: 10.1109/16.464407.

[30] Wilfried Hortschitz. 'Hybrid MOEMS Displacement Sensor and Accelerometer. Sensing Concept, Design and Technology'. PhD thesis. Institute of Sensor and Actuator Systems, TU Wien, 2013.

[31] Mark Johnson. *Photodetection and Measurement: Maximizing performance in optical systems*. New York: McGraw-Hill, 2003.

[32] Tony Wang and Barry Erhman. *Compensate Transimpedance Amplifiers Intuitively*. Tech. rep. Texas Instruments, 2005.

[33] W Hortschitz et al. 'Optical MEMS Vibration Sensor'. In: *2010 IEEE Sensors*. IEEE Sensors 2010 Conference. Nov. 2010. DOI: 10.1109/icsens.2010.5689901.

[34] Wolfgang Demtröder. *Experimentalphysik 1. Mechanik und Wärme*. Springer-Verlag Berlin Heidelberg New York, 2003.

[35] H. Steiner et al. 'Impact of a Non-linear Transfer Characteristic on the Evaluation of Static Displacements with a MOEMS Transducer'. In: *Procedia Engineering* 168 (2016), pp. 1219–1222. DOI: 10.1016/j.proeng.2016.11.421.

[36] Jörg Encke et al. 'A miniaturized linear shaker system for MEMS sensor characterization'. In: *Smart Sensors, Actuators, and MEMS VI*. Ed. by Ulrich Schmid, José Luis Sánchez de Rojas Aldavero and Monika Leester-Schaedel. SPIE, May 2013. DOI: 10.1117/12.2017405.

[37] O. Llopis et al. 'Photodiode 1/f noise and other types of less known baseband noises in optical telecommunications devices'. In: *2013 22nd International Conference on Noise and Fluctuations (ICNF)*. IEEE, 2013. DOI: 10.1109/icnf.2013.6579014.

[38] S. Pralgauskaitė et al. 'Reliability investigation of light-emitting diodes via low frequency noise characteristics'. In: *Microelectronics Reliability* 55 (Aug. 2015), pp. 52–61. DOI: 10.1016/j.microrel.2014.09.027.

Eidesstattliche Erklärung

Hiermit erkläre ich, dass die vorliegende Arbeit gemäß dem Code of Conduct, insbesondere ohne unzulässige Hilfe Dritter und ohne Benutzung anderer als der angegebenen Hilfsmittel, angefertigt wurde. Die aus anderen Quellen direkt oder indirekt übernommenen Daten und Konzepte sind unter Angabe der Quelle gekennzeichnet. Die Arbeit wurde bisher weder im In- noch Ausland in gleicher oder ähnlicher Form in anderen Prüfungsverfahren vorgelegt.

Ort, Datum

Unterschrift (Günter Hammer)